

Check for updates

RESEARCH ARTICLE

Optimizing Control and Efficiency of Two-Phase Interleaved Buck Converter With Cuckoo Search MPPT for Solar-Powered Battery Energy Storage Systems

¹Clean Technology Impact Lab, Taylor's University, Subang Jaya, Selangor, Malaysia | ²Centre for Sustainable Societies, Taylor's University, Selangor, Subang Jaya, Malaysia | ³Department of Electrical and Electronics Engineering, University College of Engineering Kancheepuram (A Constituent College of Anna University Chennai), Kancheepuram, India | ⁴Department of Electrical and Electronics Engineering, Universiti Tenaga Nasional, Kajang, Selangor, Malaysia

Correspondence: Chockalingam Aravind Vaithilingam (aravindcv@ieee.org; chockalingamaravind.vaithilingam@taylors.edu.my)

Received: 25 October 2024 | Revised: 21 April 2025 | Accepted: 24 May 2025

Funding: This work was supported by Taylor's University, TUFR/2017/001/01.

Keywords: battery charger | constant current (CC) charging | off-grid BESS charging | PV-based BESS charging | two-phase interleaved buck converter

ABSTRACT

The increasing demand for efficient energy storage in renewable energy systems has led to advancements in Battery Energy Storage Systems (BESS). This study examines the charging dynamics and thermal behavior of a BESS powered by a solar-driven two-phase interleaved buck converter (IBC). Under full load conditions, the IBC maintained a balanced current distribution between its two inductors, each carrying an average of ~11 A, with minor fluctuations ranging from 10.2 A to 11.0 A. The converter achieved a stable output voltage of 24.372 V and delivered 21.28 A to charge a BESS configured in a 788P arrangement of 18650 NMC lithium-ion cells, totaling 24 V and 20 Ah capacity. While the interleaving technique effectively reduced ripple and ensured efficient charging, thermal monitoring revealed a significant temperature increase from 27.25°C at ambient conditions to 55.85°C by the end of the charging cycle. This highlights the necessity of improved thermal management strategies to sustain battery performance and longevity. Future work should focus on refining control algorithms for current balancing, optimizing maximum power point tracking (MPPT) techniques, and enhancing thermal dissipation methods to ensure safe and efficient BESS operation in solar applications.

1 | Introduction

Escalating concerns about air pollution and its significant impact on public health, including preterm births and millions of deaths, have highlighted the necessity for cleaner transportation solutions [1]. In response to growing environmental awareness, there has been a considerable push toward EVs, including HEVs, BEVs, and PEVs [2]. Notably, despite the challenges posed by the COVID-19 pandemic, global EV sales surged by 43% in 2019 and 2020 [3]. As the demand for EVs is projected to

rise from 3.1 million in 2020 to 14 million by 2025, developing robust charging infrastructure has become increasingly critical [4]. Central to this infrastructure is the efficient management and conversion of energy to facilitate the rapid charging of energy storage systems.

To enable dependable and effective EV charging in off-grid situations, PV charging infrastructure must be integrated with BESS. PV systems, while sustainable, are inherently intermittent due to daily cycles and weather variability, rendering them inappropriate

© 2025 John Wiley & Sons Ltd.

for direct quick charging of EVs. BESS serves as a vital buffer, storing excess energy during peak solar hours and dispensing it as needed, thus separating the electric vehicle charging process from real-time solar generation. This intermediary position is particularly crucial for establishing quick charging capabilities, which demand high power output that may surpass immediate PV generation. By using BESS, the system can maintain a steady high-power output for EV rapid charging, irrespective of current solar conditions. Moreover, BESS ensures consistent voltage and current for the charging process. The BESS also optimizes the consumption of solar energy by decreasing curtailment during lowdemand periods and provides ancillary services such as power quality improvement and load balancing. Consequently, the synergy between PV and BESS not only boosts the dependability and availability of EV charging infrastructure in off-grid regions but also maximizes the consumption of renewable energy, contributing to a more sustainable and efficient transportation ecology.

The work presents the design and implementation of a compact, scalable two-phase interleaved buck converter (IBC) tailored for high-current BESS charging applications. The converter is sized to meet laboratory constraints while maintaining real-world relevance and flexibility. Operating at an output of 24.372V and 21.28 A, the IBC employs interleaving to significantly reduce current ripple, balance inductor currents, and minimize thermal stress on components. The integrated hardware prototype demonstrates efficient, stable performance under full-load conditions, providing a practical, laboratory-validated solution for solar-powered energy storage systems.

1.1 | Role of Maximum Power Point Tracking for Maximum Energy Production

MPPT is an essential technology employed in renewable energy systems, namely solar PV systems, to optimize energy generation from existing resources. The primary role of MPPT is essential for optimizing solar PV system performance by continuously adjusting the operating point to ensure maximum power output under

varying environmental conditions. Fluctuations in sunlight intensity and temperature significantly impact the electrical characteristics of solar panels, and MPPT effectively compensates for these changes in real-time, thereby improving energy efficiency. By dynamically optimizing the electrical operating point, MPPT minimizes energy losses and maintains peak performance. This functionality is critical for maximizing energy capture, particularly in environments where solar irradiance varies, or shading occurs intermittently. Additionally, MPPT demonstrates adaptability to system modifications, such as changes in panel configuration or orientation, ensuring long-term operational efficiency. In off-grid systems with energy storage, MPPT plays a pivotal role in efficiently charging batteries, maximizing the use of generated solar energy and enabling reliable power availability during periods without sunlight. The flexibility and responsiveness of MPPT make it indispensable for enhancing the overall efficiency and sustainability of solar PV systems [5-7]. The MPPT can be operated in two modes: open loop and closed loop. In an open loop system, inputs such as date, time, and position are provided, and appropriate algorithms are employed to carry out maximum tracking operations. On the other hand, in a closed-loop system, feedback systems such as LDR, cameras, and photodiodes can enable controllers to execute closed-loop operations, as shown in Figure 1.

The categorization of MPPT approaches is based on their tracking methods, which can be classified into four primary types: classical, intelligent, optimization, and hybrid. The efficacy of each tracking technique relies on its capacity to monitor maximum power output amidst changing environmental conditions. Many researchers have investigated different MPPT methods given in Table 1.

1.2 | Role of DC-DC Converter

High-performance converters are essential for harnessing energy from renewable sources, such as solar panels [36]. These converters must minimize energy losses while maximizing power transfer, which is crucial for meeting the growing energy demands of EVs. The design of such converters typically

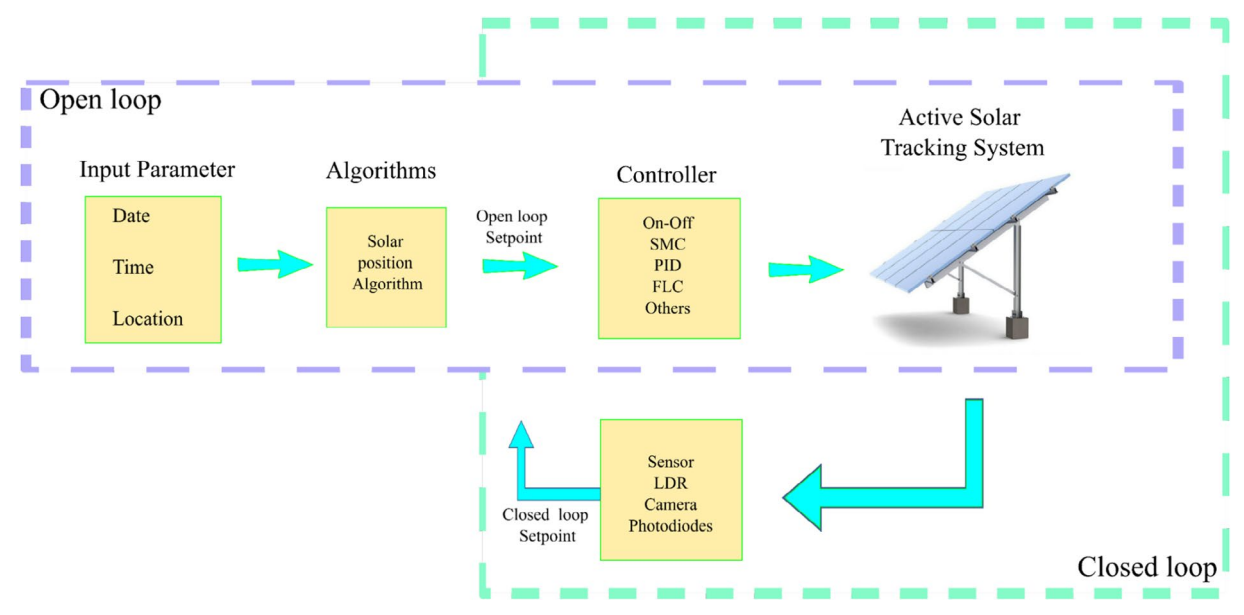


FIGURE 1 | Methodical depiction of both closed- and open-loop MPPT systems.

TABLE 1 | Various MPPT techniques.

Type	Technique	Advantages	Limitation
Traditional	P&O [8]	Simple implementation, cost-effective	Oscillations around MPPT, slower response to changing conditions
	IC [9]	Better response to irradiance changes, reduced oscillations	More complex and costly than P&O, sensitive to noise
	FOCV [10]	Simple implementation, suitable for varying temperatures	Less accurate in non-ideal conditions, slower response
	CV [11]	Simple, easy to implement	Less efficient in variable weather, not suitable for all PV types
	HC [12]	Improved efficiency compared to P&O	Sensitive to perturbations, may not converge under certain conditions
	MPC [13]	High accuracy, suitable for complex dynamics	Increased complexity and cost, require a good system model
	FLC [14]	Adaptive, robust performance	Design complexity requires tuning for optimal performance.
	Neural Network-Based MPPT [15]	Adaptive, self-learning, high accuracy potential	Complex training, limited interpretability
	Voltage-Mode MPPT [16]	Simple, widely used	Less efficient under partial shading, poor adaptability to changes
	Current-Mode MPPT [17]	Improved efficiency under specific conditions	Limited applicability, may need additional sensors.
Classical	HC [18]	Simple, fast-tracking, robust	Local maxima issues, slow convergence, noise sensitivity
	SCC [19]	High accuracy, cost-effective	Limited applicability, high voltage restrictions
	OCV [20]	Simple, robust, high accuracy	Inefficient, slow response, limited by voltage/size
Optimized	PSO [21]	Simple, high convergence, global optimization, robust	Sensitive to initial conditions, parameter selection, local optima
	GWO [22]	Global optimization, fast convergence, simple	Initial sensitivity, complexity, reliance on random search
	ACO [23]	Robust, fast convergence, global optimization	Complex, memory issues
	Cuckoo Search [24]	Global optimization, fast convergence, robust	Initial sensitivity, complex, intensive computation
	ABC MPPT [25]	Global optimization, real-time operation, noise resilience	Slow convergence, parameter sensitivity, memory-intensive
	Gauss-Newton MPPT [26]	Simple, fast MPP tracking, low sensitivity to noise	Convergence issues, impacted by initial guess

(Continues)

TABLE 1 (Continued)

Type	Technique	Advantages	Limitation
Intelligent	SMC [27]	Rapid response, high accuracy in nonlinearities	Complex control, high computation demands, chattering issues
	ANN [28]	High accuracy, handles nonlinearity well	High computational power, overfitting risk, less suitable for low power
	Fibonacci Series-Based MPPT [29]	Oscillation reduction, simple control	Sensitive to temperature, ineffective under rapid temperature changes
	DISMC [30]	Quick convergence, improved tracking	Complex modeling, prone to chattering, parameter sensitivity
Hybrid	FPSO [31]	Efficient MPP tracking, adaptable, fast convergence	Computationally intensive, stochastic processes, parameter dependency
	ANFIS [32]	Handles nonlinearity, robust to environmental changes, quick response	Computationally demanding, prone to overfitting, parameter sensitivity
	GWO-P&O [33]	Fast convergence, global optimal solution	Increased complexity, initial sensitivity, and high computation demands
	PSO-P&O [34]	Fast convergence, global MPP, robust to variations	Computational demands, sensitive to parameters and initial conditions
	HC-ANFIS [35]	High tracking accuracy, robust, quick response	High computational power, overfitting, initial condition sensitivity

emphasizes optimizing current flow and reducing ripple, thus enhancing efficiency and extending the overall longevity of the system [37]. Power converters play a pivotal role in managing energy flow, converting electrical energy from one form to another while maintaining high efficiency and performance. As the landscape of energy applications evolves, various converter topologies have been developed to meet the diverse requirements of different sectors, including consumer electronics, automotive, and industrial applications [38]. Each topology comes with its unique set of characteristics, advantages, and challenges. Understanding these parameters is crucial for selecting the appropriate converter for specific applications.

Converter topologies have emerged, each offering unique characteristics and benefits tailored for specific applications. The LLC Resonant Converter features soft switching capabilities with a component count of two inductors, nine capacitors, five switches, and four diodes, achieving 3 kW at 100 kHz with an output voltage of 400 V. While it offers a wide load range and reduced voltage stresses due to its cascade switch structure, it does require high-efficiency data and presents control complexity along with a high component count [39]. The Quasi-Resonant Interleaved Flyback Converter, comprising 0 inductors, 24 capacitors, 2 switches, and 12 diodes, boasts a bidirectional capability and operates at 2 kW with a frequency of 65 kHz. This converter effectively employs soft switching during low-voltage

operation and can absorb excess energy, yet it faces challenges with high control complexity [40].

In contrast, the Modular Dual Active Bridge Converter, with its configuration of 6 inductors, 1 capacitor, and 16 switches, supports high power levels of up to 20 kW at a frequency of 50 kHz, delivering 800 V. It is well-suited for wide load ranges, but the potential for voltage spikes due to transformer leakage inductance is a noted disadvantage [41]. The PV-fed SEPIC Converter has a more straightforward design, incorporating three inductors, three capacitors, one switch, and one diode, with an output of 1 kW at $100\,\mathrm{kHz}$ and an output voltage of 48 V. This topology is particularly advantageous for PV applications, yet it experiences increased control complexity under varying irradiance conditions [42].

Enhancing the previous design, the PV-fed SEPIC with a Backup Battery-fed Interleaved Bidirectional Converter exhibits a higher power rating of 5kW at 150kHz, operating between 60 and 400 V. With a simple design and efficient performance under dynamic irradiation, its complexity rises when integrating both PV and battery systems [43]. The Multilevel LLC Converter, although needing two different DC input supplies, offers a transformerless design that significantly reduces costs. Its efficiency, around 97%, and capability for high-frequency operation make it appealing, despite the challenges of a high switch count and complex soft-switching control [44].

The two-phase Interleaved Boost Converter (IBC), designed for high-power operations ranging from 16 to 32 kW at frequencies between 20 and 40 kHz, excels in reducing current ripple but suffers from high voltage stresses across its switches and lacks isolation [45]. Similarly, the 3-phase Interleaved Converter, rated for 100kW at 25kHz, presents high efficiency for demanding applications but necessitates complex control strategies, particularly when scaling up for multiple phases [46]. The Parallel 3-level Converter with Separate Inductors and the 3-level Asymmetrical Voltage Source Converter both cater to specific load conditions, with the latter being particularly suited for vehicle-to-grid (V2G) applications. While offering flexibility, both face challenges in terms of control complexity and high switch counts [47, 48]. Notably, the ZVT Converter and its variants like the IZVT Converter and Half-Bridge ZVT Converter emphasize reduced voltage stress across switches. Despite their benefits for high-power applications, they introduce higher control complexity and potential losses [45]. Lastly, the 3-level ZVT Converter is optimized for high-power applications, achieving an impressive efficiency of 98% at 300 kHz, though it lacks isolation, complicating control and management of switching losses [49]. A detailed comparative analysis is provided in Table 2.

The manuscript presents a comprehensive approach to solarpowered battery charging, emphasizing several distinct contributions. Unlike many studies that utilize resistive loads or current sources to simulate battery charging, this work implements a real 7S8P NMC lithium-ion battery pack, offering a more accurate and practical assessment of charging dynamics. The Cuckoo Search Algorithm is integrated for MPPT, optimizing power extraction under real-time irradiance conditions that account for intermittency and transient variations during the charging cycle, further distinguishing this study from others. Additionally, the two-phase interleaved buck converter is deployed to enhance current balancing and minimize ripple, while a detailed experimental validation from no-load to full-load operation ensures robust performance evaluation. The efficiency of the system is rigorously selfvalidated through theoretical, simulated, and experimental results, making this study a holistic and realistic exploration of solar-powered BESS charging.

The remaining manuscript presents a comprehensive study of the design, development, and analysis of a solar-powered BESS using a two-phase IBC. It begins with the methodology for implementing a Cuckoo Search Algorithm-based MPPT system, followed by a numerical analysis of the two-phase IBC. The development of a solar-powered BESS prototype is detailed, alongside an efficiency analysis. The results section includes both simulation and experimental data for the two-phase IBC, covering its output characteristics and efficiency, and concludes with the charging characteristics of the BESS.

2 | Methodology

2.1 | CSA-Based MPPT Tracking

The CSA algorithm is inspired by the brood parasitism behavior observed in certain cuckoo species. These birds lay their eggs in the nests of other bird species. In response, the host

bird may reject the cuckoo egg by either discarding it or abandoning the nest. However, some species, such as Tapera, have evolved to produce eggs that closely mimic the color and pattern of the host bird's eggs. Drawing from this natural behavior, the algorithm was developed in 2009 by [50]. The governing equations for obtaining MPP are given in Equations (1-4) and shown in Figure 2. The CSA algorithm for MPPT operates by treating each nest as a candidate duty cycle for the converter. Initially, a set of nests (duty cycles) is randomly generated, and the corresponding power outputs are evaluated. The algorithm follows an exploration-exploitation approach, where new duty cycles are generated using Lévy flights, enabling large jumps to explore a wider range. Each new duty cycle replaces an existing one only if it yields higher power output, ensuring continuous improvement. Over iterations, the nests converge toward the duty cycle that maximizes PV power. When irradiance or temperature changes, the algorithm dynamically adjusts by redistributing nests and re-evaluating power levels, allowing it to quickly track and adapt to the new maximum power point. The CSA algorithm's ability to balance exploration (global search) and exploitation (local refinement) makes it highly effective for tracking under rapidly varying conditions.

$$V_j^{i+1} = V_j^i + \alpha. Levy = V_j^i + s$$
 (1)

$$s \approx K. \left(\frac{u}{|v|^{\frac{1}{\beta}}}\right) \left(V_{best} - V_j\right)$$
 (2)

$$u \approx N(0, \sigma_u^2); v \approx N(0, \sigma_u^2)$$
 (3)

$$\sigma_{u} = \left(\frac{\gamma(1+\beta) * \sin(\pi+\beta/2)}{\gamma\left(\frac{(1+\beta)}{2}\right) * \beta * \left(2^{\frac{\beta-1}{2}}\right)}\right)^{\frac{1}{\beta}}; \sigma_{v} = 1 \tag{4}$$

2.2 | Numerical Analysis of Two-Phase IBC

This study deviates from the typical use of boost converters for increasing voltage levels by examining the application of a two-phase IBC for standalone solar-powered EV charging stations. The decision is not based on the idea that one topology is obsolete or unexplored, but rather on the practical limitations of reducing the size to laboratory prototypes. In these prototypes, lower voltage profiles are more common, making buck converters more appropriate. This research seeks to explore the possible benefits of using IBCs in this specific application by including the CSA algorithm.

The choice of converter topology has a substantial impact on the overall efficiency and efficacy of solar-powered BESS charging solutions. IBCs have gained interest because they can evenly transfer current over numerous phases, resulting in reduced ripple currents, less I²R losses, and improved system efficiency. Due to this intrinsic benefit, they are highly suitable for applications that require low voltage profiles, such as laboratory-scale prototypes of standalone solar-powered BESS charging systems. The IBC and CSA are numerically analyzed using MATLAB, which allows for an accurate assessment of converter efficiency, current ripple, and voltage regulation under dynamic operating conditions. The CSA is verified for optimizing control settings

 $\textbf{TABLE 2} \hspace{0.2cm} | \hspace{0.2cm} A \hspace{0.1cm} \textbf{detailed comparative analysis of DC-DC converters applicable to high-current applications.} \hspace{0.2cm}$

References	Topology	Component count (L CSDTr)	Power (kW)	Freq. (kHz)	Output voltage (V)	Efficiency (%)	Modulation	Features	Limitations
[39]	LLC Resonant Converter	2L, 9C, 5S, 4D, 1Tr	m	100	400	94	PWM	Suitable for wide load ranges	Needs higher efficiency data Component count optimization Increased control complexity
[40]	Quasi-Resonant Interleaved Flyback Converter	0L, 24C, 2S, 12D, 0Tr	И	65	300	92	Critical Conduction Mode	Soft switching Resonant converters absorb excess energy	 Soft switching only through low voltage switching during charging, not at zero point Higher control complexity
[41]	Modular Dual Active Bridge Converter	6L, 1C, 16S, 0D, 3Tr	20	50	800	93	Phase-Shift Modulation	Suitable for a wide load range.	 Switch count may be optimized. Transformer leakage inductance may result in voltage spikes across switches.
[42]	PV-fed SEPIC Converter	3L, 3C, 1S, 1D, 0Tr	П	100	84	95	PWM	 Suitable for PV applications. 	• Increased control complexity
[43]	PV-fed SEPIC with Backup Battery- fed Interleaved Bidirectional Converter	7L, 10C, 2S, 10D, 1Tr	٠.	150	60-400	96	PWM	 High efficiency for dynamic irradiation conditions. 	• Increased control complexity
[44]	Multilevel LLC Converter	2L, 4C, 8S, 4D, 0Tr	20	100	450	97	PWM	High-frequency operation	 Requires two different DC input supplies High switch count Increased frequency selectivity for soft switching
[45]	2-phase IBC	4S, 0D	16–32	20-40	350	98.5	PWM	Suitable for high- power operations	High voltage stresses across switches Absence of isolation

(Continues)

Energy Storage, 2025

TABLE 2 | (Continued)

		Component count (L	Power	Freq.	Output voltage	Efficiency			
References	Topology	CSDTr)	(kW)	(kHz)	3	(%)	Modulation	Features	Limitations
[46]	3-phase Interleaved Converter	6S, 0D	100	25	450	86	PWM	High efficiency.	Complex control strategies
[47]	Parallel 3-Level Converter with Separate Inductors	8S, 0D	1.2	4.32	400	96	PWM	High flexibility and low component count.	• Complex control systems
[48]	3-level Asymmetrical Voltage Source Converter	4S, 0D	40	20	200–500	97	PWM	• Suitable for V2G.	High switch count and complex control
[45]	ZVT Converter	4S, 0D	8.5	220	400	96	PWM	• Reduced voltage stress.	 High power losses in high-power applications Complex control
[45]	IZVT Converter	6S, 0D	1	70-400	300	95	PWM	 High efficiency for medium-power applications. 	 High control complexity for high-power applications
[45]	Half-Bridge ZVT Converter	4S, 0D	100	8.5	250	96	PWM	• Reduced switching losses at high power	 High power losses in high-power applications
[49]	3-level ZVT Converter	6S, 0D	100	300	800	86	PWM	 High efficiency for high-power applications. 	• Lacks isolation

25784862, 2025, 5, Downloaded from https://onlinelibrary.wiley.com/doi/10.1002/est2.70213 by Guangst University, Wiley Online Library on [19/06/2025]. See the Terms and Conditions (https://onlinelibrary.wiley.com/terms-and-conditions) on Wiley Online Library for rules of use; OA articles are governed by the applicable Cerative Commons License

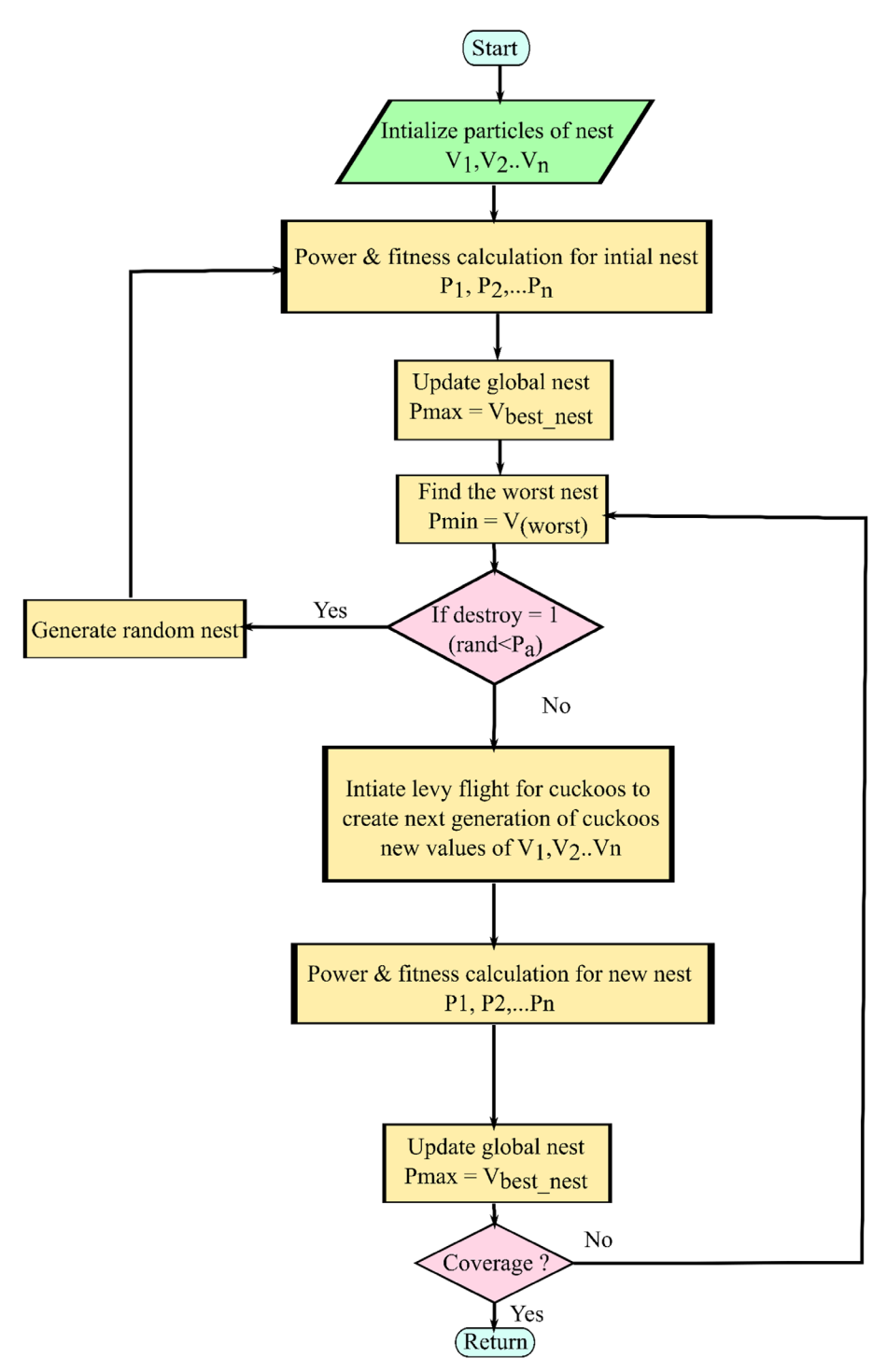


FIGURE 2 | Systematic flowchart of Cuckoo search-based MPP tracking [51].

to improve system stability and MPPT convergence, while the IBC's interleaving technique can be evaluated for current balancing through simulation. In-depth performance analysis is made possible by MATLAB's computational tools, which guarantee that the CSA achieves strong real-time control adaptability and that the IBC runs effectively with little ripples. Furthermore, the incorporation of optimization methods such as the CSA algorithm improves the efficiency of IBCs by adjusting system parameters and maximizing energy utilization. Two-phase IBC topology and its specification are shown in Figure 3, Table 3 and its modes of operation are given in Table 4.

In the solar PV panel model, temperature and irradiation are the two main inputs that affect the panel's output characteristics. The solar panel uses these inputs to generate the voltage $V_{\rm PV}$ and current $I_{\rm PV}$, which are crucial parameters for the CSA-based MPPT algorithm. The CSA uses $V_{\rm pv}$ and $I_{\rm pv}$ to calculate the ideal duty cycles needed to match the reference current profile. An appropriate load resistor is added at the output to simulate changing load conditions and make sure the reference current profile is successfully maintained. This configuration offers an adaptive and effective control mechanism for real-time optimization of the solar PV system under changing environmental conditions.

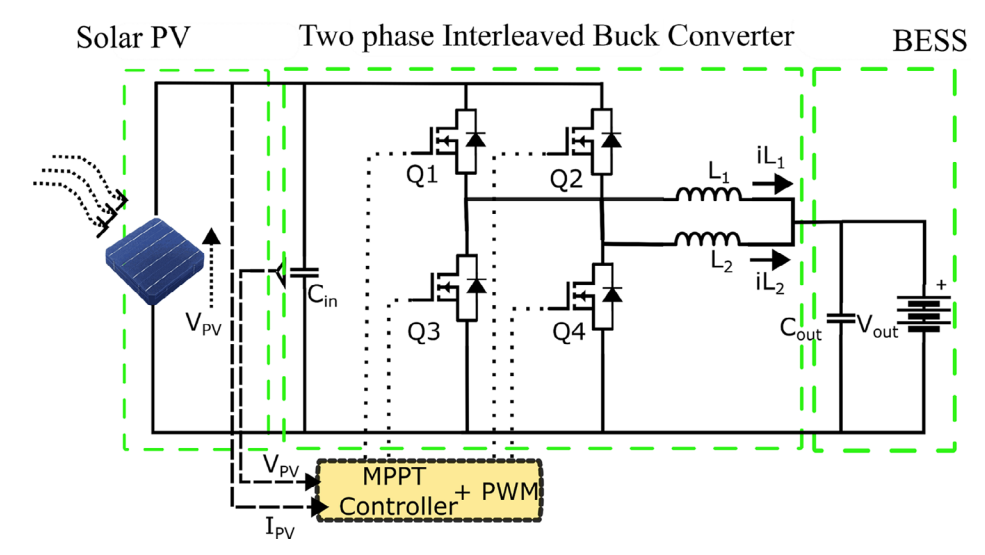


FIGURE 3 | Schematic diagram of two-phase IBC.

TABLE 3 | Design specification of two-phase IAB.

Parameter	Specifications	Unit
Solar panel output voltage	30-60	V
BESS nominal voltage	24	V
BESS capacity	480	Wh
Rated maximum current	20	A
Switching frequency	180	kHz
Inductor (L1 and L2)	22	μH
Capacitor (C_{in} and C_{out})	100, 1000	V, pF
MOSFETS (Q1, Q2, Q3, and Q4)	100	V

TABLE 4 | Two-phase IBC's operating modes.

	Mode 1	Mode 2	Mode 3	Mode 4
V_{L1}	$V_{pv}-V_{out}$	$-V_{out}$	-V _{out}	-V _{out}
\boldsymbol{V}_{L2}	$-V_{out}$	$-V_{out}$	$V_{pv}-V_{out}$	$-V_{out}$
$rac{d}{dt}i_{L1}$	1	\downarrow	1	\downarrow
$rac{d}{dt}\dot{t}_{L2}$	1	1	↓	\downarrow
$rac{d}{dt}i_{L0}$	↑	\downarrow	1	\downarrow

Note: †increasing; ↓ decreasing.

The synchronous two-phase IBC emerges as a significant topology. Illustrated in the accompanying figure, the IBC configuration comprises several essential components, including $V_{\rm PV}$ as the input voltage source, $V_{\rm out}$ as the output voltage, and four MOSFETs $(Q_1,\,Q_2,\,Q_3,\,Q_4)$ acting as synchronous switches. Additionally, two inductors, denoted L_1 and L_2 , are connected in parallel, while input and output filters, denoted Cin and Cout respectively, serve to smoothen voltage ripples. Notably, the converter interfaces with a battery acting as a load, ensuring a seamless energy transfer process.

At the heart of the synchronous two-phase IBC lies its ability to efficiently step down voltage levels while simultaneously leveraging the advantages of synchronous rectification. The operation of the converter is orchestrated by a microcontroller, which supplies pulse width modulation (PWM) signals to the four MOSFETs. These PWM signals govern the switching behavior of the MOSFETs, thereby regulating the flow of current through the inductors \mathbf{L}_1 and \mathbf{L}_2 . This synchronous interleaving of the phases ensures that the current ripple is distributed across both inductors, thereby reducing overall ripple current and improving system efficiency.

During operation, when the switches Q_1 and Q_4 are closed while Q₂ and Q₃ remain open, current flows through inductor L₁, establishing a magnetic field. Simultaneously, the voltage difference between \boldsymbol{V}_{PV} and \boldsymbol{V}_{out} is applied across the inductors in the forward direction which is V_L is given in Equation (5), facilitating energy transfer. Conversely, when the switches Q2 and Q3 are closed and Q_1 and Q_4 are open, a similar process occurs in inductor L_2 . The increase in inductor current until the end of conduction period is given in Equation (6) and (7). When the switches are turned off, the current direction remains the same and load is supplied by inductor current followed by a decrease in inductor current till the end of the off period and its corresponding Equations are given in (8) and (9). Under steady-state conditions, the energy stored in the inductor is same from the one period to another which makes the inductor current is same at the beginning and the end which was given in (10) and solved to get Equation (13).

$$V_L = V_{PV} - V_{out} = L. \frac{di_L(t)}{dt}$$
 (5)

$$\int_{0}^{T_{on}} di_{L}(t) = \int_{0}^{T_{on}} \frac{V_{PV} - V_{out}}{L} \cdot dt$$
 (6)

$$i_L(T_{on}) - i_L(0) = \frac{V_{PV} - V_{out}}{L} \cdot T_{on}$$
 (7)

$$\int_{T_{on}}^{T} di_{L}(t) = \int_{T_{on}}^{T} \frac{V_{PV} - V_{out}}{L} . dt$$
 (8)

$$i_L(T) - i_L(T_{on}) = -\frac{V_{out}}{L} \cdot (T - T_{on})$$
(9)

$$i_L(0) = i_L(T) \tag{10}$$

$$i_L(0) = i_L \left(T_{on}\right) - \left(\frac{V_{PV} - V_{out}}{L}\right). T_{on} \tag{11} \label{eq:ill}$$

$$i_L(T) = i_L(T_{on}) + \left(\frac{V_{out}}{L}.(T_{on} - T)\right)$$
 (12)

$$\left(\frac{V_{PV} - V_{out}}{L}\right) \cdot T_{on} = \frac{V_{out}}{L} \cdot \left(T_{on} - T\right)$$
 (13)

As the interleaved inductors are not coupled their current ripples can be calculated as Equations (14-16) with T being the switching period. As the output current increases in Mode 1 and Mode 3 and decreases in Mode 2 and Mode 4, the output ripple occurs two times in the provided switching cycle. Therefore, the change in output ripple current can be calculated as Equations (14-17).

$$\Delta i_{L1} = \frac{V_{out}}{L_1} (1 - D)T \tag{14}$$

$$\Delta i_{L2} = \frac{V_{out}}{L_2} (1 - D)T \tag{15}$$

$$\Delta i_L = \frac{V_{out}}{L} (1 - D)T \tag{16}$$

$$\Delta i_{L_{out}} = \frac{V_{out}}{L} (1 - 2D)T \tag{17}$$

2.3 | Design and Development of a Prototype for Solar-Powered BESS System

The process of creating a prototype for a standalone solar-powered BESS consists of developing a DC-DC two-phase IBC, which entails the tasks of designing, constructing, and evaluating a power conversion circuit that effectively reduces the voltage from a higher level to a lower level to charge the BESS. A layout for a PCB is created to reduce parasitic inductance and capacitance, while also providing efficient thermal control. Subsequently, the PCB is manufactured, and the components are meticulously integrated, ensuring high-quality soldering and precise component positioning. The design of the two-phase IBC is to operate with solar panel modules ranging from 30 to 60 V and can accommodate battery systems of 24 V, delivering an output current of up to 20 amps.

The converter employs the CSA algorithm for MPPT, achieving an operational efficiency exceeding 96%. This efficiency reflects the losses associated with battery reverse polarity protection and panel reverse flow protection, both managed by MOSFETs (CSD18540Q5B). The high efficiency achieved is primarily due to the use of low gate charge MOSFETs (CSD19531Q5A) and the interleaved buck topology integrated into the design. Furthermore, the system's high operating frequency, reaching up to 200 kHz per stage, enables the use of smaller components, which further improves the design's overall efficiency and

TABLE 5 | System specifications.

Parameter	Specifications	Unit
Solar panel input voltage	30-60	V
BESS nominal voltage	24	V
Rated maximum current	20	A
MPPT efficiency	96	%
Switching frequency	180	kHz

performance. The system specifications for the design and development of two-phase—IBC are given in Table 5 and the overall block diagram of two-phase IBC is given in Figure 4.

Voltage and current measurements from both the panel and battery lines are used to calculate and monitor the MPPT. The MSP430 microcontroller enables rapid data acquisition by utilizing its internal ADC, which samples these analogue signals every 1.3 ms. Operating at 25 MHz, this setup allows for fast conversion and computation, enhancing MPPT efficiency and facilitating real-time adjustments to the output of the IBC.

During battery charging, the MSP430 generates PWM signals to control the IBC, with the duty cycle of the PWM signals directly influencing the output current, which corresponds to the battery charging current. Additionally, the MCU regulates battery voltage, preventing overcharging by disabling the buck converter once a preset voltage threshold is reached. Primarily 18 650 cells are used to construct the battery pack, the focus is to investigate the application of PV-based charging and its impact on temperature dynamics during the charging of BESS. The properties of the 18 650 NMC cell under study are given in Table 6.

2.4 | Efficiency Analysis

Efficiency analysis is to be carried out for the active switches and inductors present in the prototype. The following equations explain the methods to calculate the power loss factors across active devices in the prototype. The nine primary sources of power loss in the system include MOSFET conduction losses $P_{\rm ON-H},\,P_{\rm ON-L},\,$ switching losses $P_{\rm SW-H},\,P_{\rm SW-L},\,$ reverse recovery losses in the body diode $P_{\rm DIODE},\,$ output capacitance losses $P_{\rm COSS},\,$ dead time losses $P_{\rm D},\,$ gate charge losses $P_{\rm G},\,$ operational losses of the IC control circuit $P_{\rm IC},\,$ inductor conduction losses $P_{\rm L(DCR)},\,$ and capacitor losses $P_{\rm CIN},\,P_{\rm COUT}.$

The conduction loss in the MOSFET is analyzed in sections A and B of the waveform depicted in Figure 5 in section A, when the high-side MOSFET is active and the low-side MOSFET is inactive, the conduction loss of the high-side MOSFET is determined by the output current, the MOSFET's on-resistance, and the on-duty cycle. In contrast, during section B, when the high-side MOSFET is off and the low-side MOSFET is active, the conduction loss of the low-side MOSFET is calculated using the output current, the MOSFET's on-resistance, and the off-duty cycle.

$$P_{ON-H} = I_{batt}^{2} \times R_{ON-H} \times \frac{V_{batt}}{V_{pv}}$$
 (18)

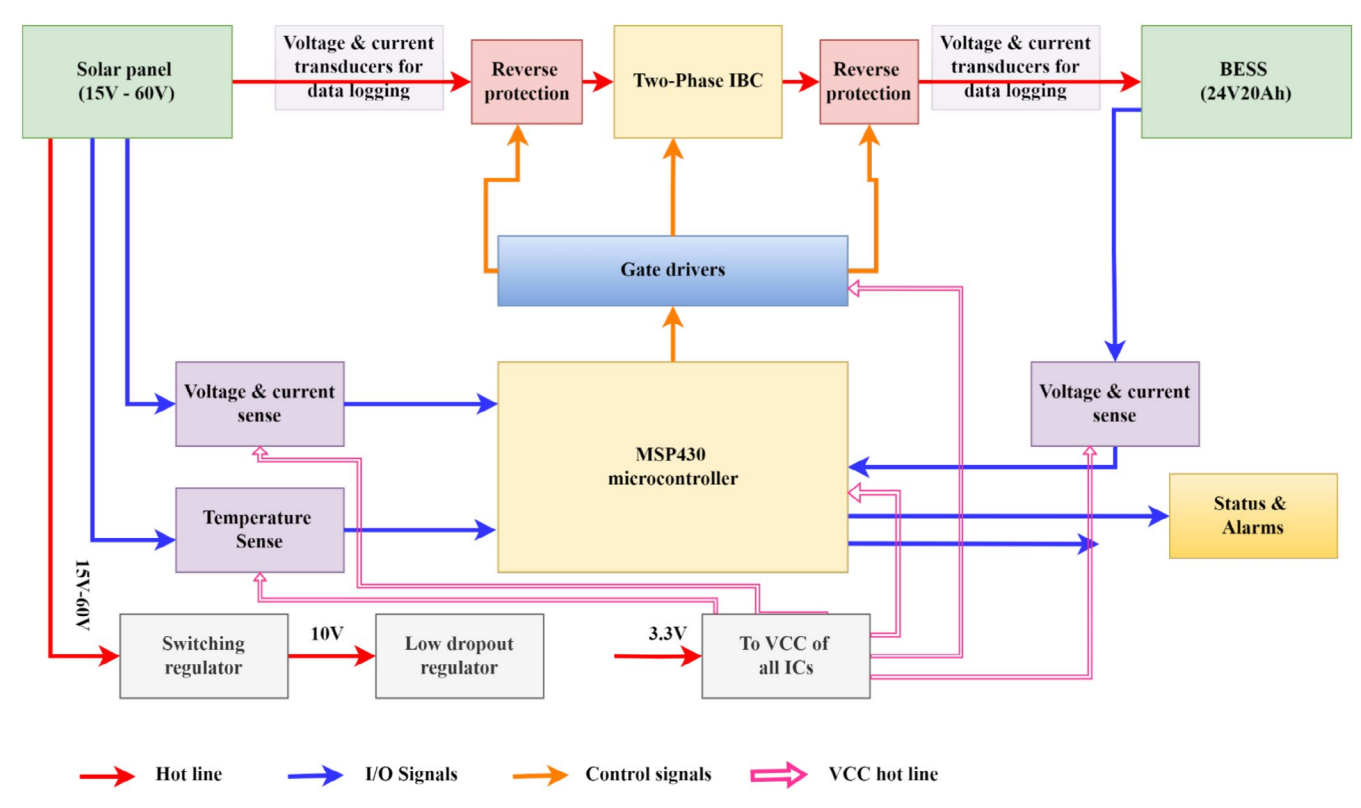


FIGURE 4 | Overall block diagram for hardware prototype of two-phase IBC.

TABLE 6 | Properties of 18 650 cell.

Parameter	Cell properties
Chemistry	NMC
Cell form factor	18650
Cathode chemistry	${\rm LiNiMnCoO}_2$
Weight	42.4 g
Nominal voltage	3.7 V
Nominal capacity	2600 mAh
Charging current continuous/peak	2.6 Ah/5.2 Ah
Total energy	7.2Wh
Full cell voltage	4.2 V
Cut-off voltage	3.1 V

2.4.1 | Low-Side MOSFET

$$P_{ON-L} = I_{batt}^{2} \times R_{ON-L} \times \left(1 - \frac{V_{batt}}{V_{pv}}\right)$$
 (19)

In Equations (18) and (19), the output current represents the average inductor current. As illustrated in the lower part of Figure 5, actual ramp waveforms incur greater losses. When the current waveform is more pronounced (with a higher peak current), the effective current is found by integrating the square of the difference between the peak and trough values of the current. This method allows for a more precise calculation of the

loss. The conduction losses P_{ON-H} , P_{ON-L} are calculated using the following Equations (20) and (21).

2.4.2 | High-Side MOSFET

$$P_{ON-H} = \left[I_{batt}^2 + \frac{\left(I_P - I_V \right)^2}{12} \right] \times R_{ON-H} \times \frac{V_{batt}}{V_{pv}} \tag{20}$$

2.4.3 | Low-Side MOSFET

$$P_{ON-L} = \left[I_{batt}^2 + \frac{\left(I_P - I_V \right)^2}{12} \right] \times R_{ON-H} \times \left(1 - \frac{V_{batt}}{V_{pv}} \right) \tag{21}$$

$$\Delta I_L = \frac{\left(V_{pv} - V_{batt}\right)}{f_{sw} \times L} \times \frac{V_{batt}}{V_{pv}}$$
 (22)

$$I_P = I_{batt} + \frac{\Delta I_L}{2} \tag{23}$$

$$I_P = I_{batt} \tag{24}$$

The switching losses are ascertained in the C and D parts, or the E and F sections, of the waveform illustrated in Figure 5. Losses transpire during the transition intervals when the high-side and low-side MOSFETs successively switch ON and OFF. The area of the two triangles created during the switching transitions is comparable to the power losses experienced during the rising

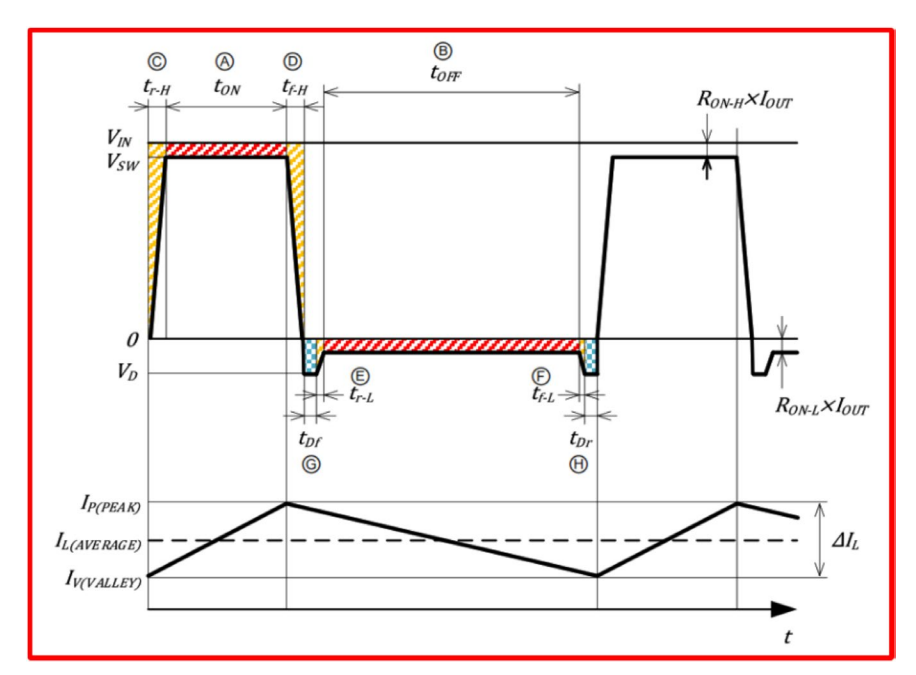


FIGURE 5 | Voltage waveform of MOSFET and current waveform of the inductor [52].

and lowering edges. Consequently, this loss can be quantified with a simple geometric formula. The switching loss, PSW-H, is determined using the subsequent equation.

2.4.4 | High-Side Metal-Oxide-Semiconductor Field-Effect Transistor

$$P_{SW-H} = \frac{1}{2} \times V_{pv} \times I_{batt} \times (t_{r-H} + t_{f-H}) \times f_{sw}$$
 (25)

2.4.5 | Low-Side MOSFET

$$P_{SW-L} = \frac{1}{2} \times V_D \times I_{batt} \times \left(t_{r-L} + t_{f-L}\right) \times f_{sw}$$
 (26)

Diode recovery results from the low-side MOSFET's body diode switching from forward conduction to reverse bias when the high-side MOSFET enters the ON state. This operation produces a reverse recovery loss in the body diode, defined by the diode's reverse recovery time t_{RR} . The loss can be computed using the Equation (27) derived from the diode's reverse recovery characteristics.

$$P_{DIODE} = \frac{1}{2} \times V_{pv} \times I_{RR} \times t_{RR} \times f_{sw}$$
 (27)

In each switching cycle, a loss occurs due to the charging of the output capacitances C_{OSS} of the high-side MOSFETs. This loss is quantified using the following equation. Typically, the charge/discharge loss of C_{OSS} in the low-side MOSFET is disregarded because the charge is already dissipated by the inductor current when the low-side MOSFET turns on, thereby achieving Zero Voltage Switching (ZVS).

$$P_{COSS} = \frac{1}{2} \times C_{OSS-H} \times V_{pv}^{2} \times f_{sw}$$
 (28)

$$C_{OSS-H} = C_{DS-H} + C_{GD-H}$$

A short circuit between V_{pv} and ground happens when the high-side and low-side MOSFETs are turned on at the same time, producing a large current spike. The implementation of a dead time, in which the inductor current flows while both MOSFETs are off, prevents such short circuits. During this dead time, the inductor current flows via the body diode of the low-side MOSFET. The dead time loss, PD, is determined in the G and H regions of the waveform in Figure 5 using the following Equation (29).

$$P_D = V_D \times I_{batt} \times (t_{Dr} + t_{Df}) \times f_{sw}$$
 (29)

The gate charge loss arises from the power consumed during the charging of the MOSFET gate. It is influenced by the gate charges, also known as gate capacitances, of both the high-side and low-side MOSFETs. This loss can be quantified using the following Equations (30).

$$P_{G} = (Q_{g-H} + Q_{g-L}) \times V_{gs} \times f_{sw}$$
(30)

$$Or P_G = (C_{GS-H} + C_{GS-L}) \times V_{gs}^2 \times f_{sw}$$
 (31)

The consumption power used by the IC control circuit P_{IC} is calculated with the following Equation (32).

$$P_{IC} = V_{pv} \times I_{CC} \tag{32}$$

There are two types of power loss connected with the inductor: conduction loss owing to resistance and core loss due to magnetic characteristics. The calculation of core loss is removed in this article due to its complexity. The DCR of the inductor's winding is the cause of conduction loss. Larger wire cross-sections result in a drop in DCR, while longer wire

lengths increase DCR. Applied to inductor components, DCR rises with greater inductance values and decreases with bigger case sizes. The conduction loss of the inductor can be computed using the following equation. The duty cycle does not affect the inductor's performance because it stays powered continuously. Because power loss is proportional to the square of the current, greater output currents lead to increased losses. Therefore, selecting adequate inductors is vital.

$$P_{L(DCR)} = I_{batt}^{2} \times DCR$$
 (33)

$$P_{L(DCR)} = \left[I_{batt}^2 + \frac{\left(I_P - I_V \right)^2}{12} \right] \times DCR$$
 (34)

Even though capacitors suffer from a variety of losses, including dielectric, leakage, and series resistance losses, these are frequently combined into a generalized loss model called ESR. The ESR is then multiplied by the square of the RMS value of the alternating current (AC) flowing through the capacitor to get the power loss inside the capacitor. Which was given in Equation (35) and the RMS current in the input capacitor can be estimated with equation (36).

$$P_{CAP(ESR)} = I_{CAP(RMS)}^{2} \times ESR \tag{35}$$

$$I_{CIN(RMS)} = I_{batt} \times \frac{\sqrt{(V_{pv} - V_{batt}) - V_{batt}}}{V_{pv}}$$
 (36)

The RMS current in the output capacitor corresponds to the RMS value of the inductor's ripple current and is determined using the following Equation (38).

$$I_{\text{COUT(RMS)}} = \frac{\Delta I_{\text{L}}}{2\sqrt{3}} \tag{37}$$

$$\Delta I_{L} = \frac{\left(V_{pv} - V_{batt}\right)}{f_{sw} \times L} \times \frac{V_{batt}}{V_{pv}}$$
(38)

The overall power loss of the system is given by Equation (39).

$$\begin{split} P &= P_{ON-H} + P_{ON-L} + P_{SW-H} + P_{SW-L} + P_{DIODE} \\ &\quad + P_{COSS} + P_D + P_G + P_{IC} + P_{L(DCR)} + P_{CIN} + P_{COUT} \end{split} \tag{39}$$

Based on the total power loss obtained in the equation in Equation (39) the overall system efficiency can be calculated by Equation (40)

$$\eta = \frac{V_{batt} \times I_{batt}}{V_{batt} \times I_{batt} + P} \tag{40}$$

The total power loss in a synchronous two-phase IBC primarily arises from semiconductor losses, inductor losses, and capacitor losses. Semiconductor losses include switching and conduction losses in both high-side and low-side MOSFETs, with additional losses during dead time and reverse recovery in the low-side MOSFET. Inductor losses encompass both DC losses, due to winding resistance, and AC losses, which are related to

core material properties and operating frequency. Capacitor losses occur in both input and output capacitors, with significant factors being ESR and the ability to handle ripple currents. Optimizing these components is essential for improving converter efficiency and reducing total power loss.

3 | Results and Discussion

3.1 | Simulation Results of Two-Phase IBC

3.1.1 | PV & IV Characteristics

The following curves Figures 6 and 7 illustrate the I–V (current-voltage) and P–V (power-voltage) characteristics of a PV system under varying irradiation levels at two distinct temperatures: 25° C and 55° C. At 25° C, the I–V curves demonstrate a clear relationship between increasing irradiation and current output, with higher irradiation levels resulting in higher short-circuit currents (I_sc). The corresponding P-V curves indicate that the MPPT shifts upwards with increasing irradiation, reflecting the enhanced power output of the PV system under higher light intensity.

At 55°C, the I-V curves also show increased current with higher irradiation, but with a noticeable reduction in open-circuit voltage (V_oc) compared to the 25°C condition. This is due to the temperature-induced reduction in the semiconductor bandgap, which lowers the V_oc. The P-V curves at 55°C confirm that while the MPP increases with higher irradiation, the overall power output is reduced compared to the 25°C condition due to the higher operational temperature. These results highlight the impact of both irradiation and temperature on the performance of PV systems. Higher irradiation improves current and power output, but elevated temperatures can diminish efficiency by reducing the open-circuit voltage and overall power generation. Understanding these dependencies is crucial for optimizing the design and operation of PV systems in varying environmental conditions.

3.1.2 | Output Characteristics of Two-Phase IBC

The results of these simulations are crucial for understanding the behavior of the IBC under different conditions. In particular, the current waveforms in the inductors reveal how interleaving helps in reducing the overall ripple, leading to a more stable and efficient power conversion process. The input current and voltage profiles Figure 8 illustrate the efficiency of the converter in drawing power from the source, while the output current and voltage curves demonstrate the converter's ability to deliver a stable and reliable output to the load.

At full load conditions, the simulation of the two-phase IBC reveals significant insights into its operational performance. The current waveforms in the two inductors are ~10.9 A each. This indicates that the interleaving technique effectively distributes the ripple current between the two phases, resulting in a substantial reduction in the overall current ripple. Such a reduction is critical for enhancing the stability and efficiency of the power conversion process. The voltage across the MOSFETs is observed to be ~28 V, which aligns with the expected operational voltage given the converter's design parameters. This

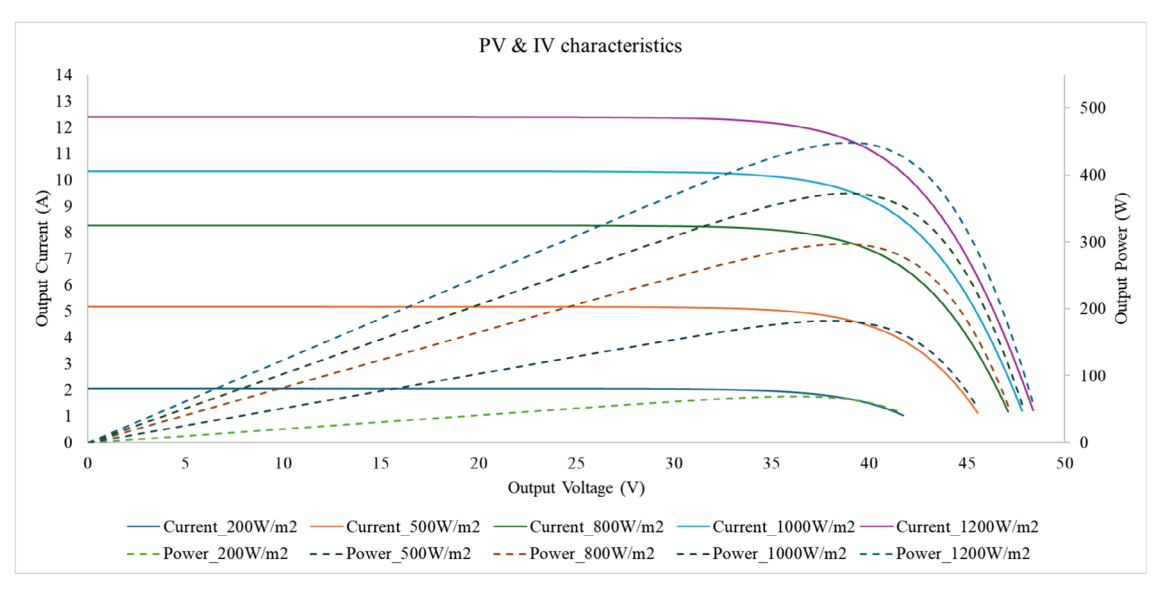


FIGURE 6 | IV and PV characteristics curve at 25°C.

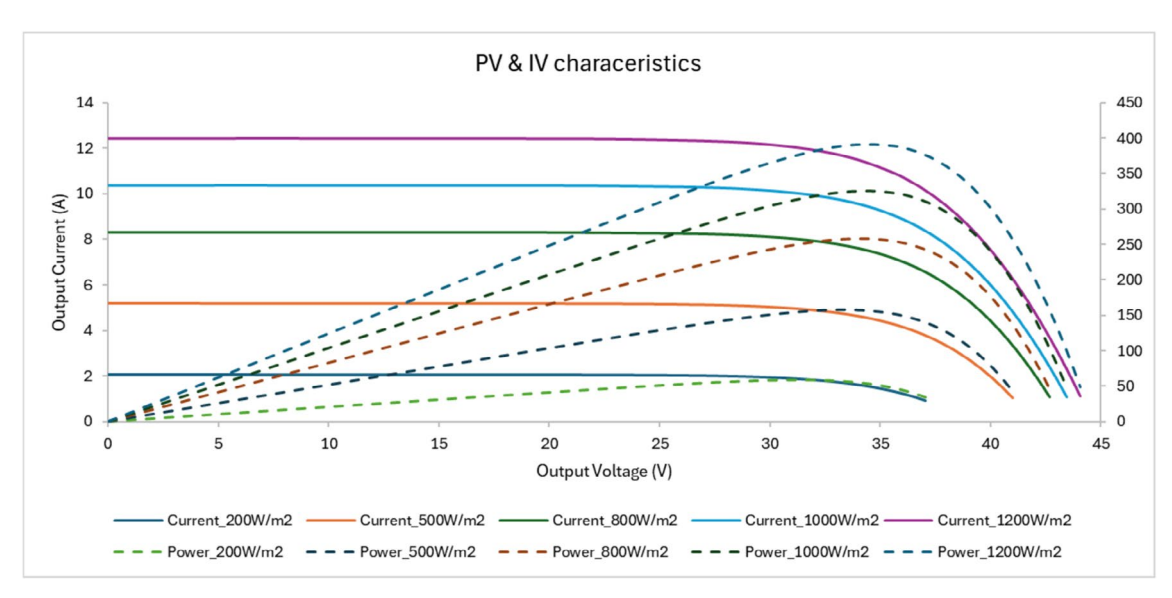


FIGURE 7 | IV and PV characteristics curve at 55°C.

consistency confirms that the MOSFETs are operating within their intended voltage range, ensuring reliable switching and minimal stress on the components.

The output characteristics of the converter are also noteworthy. The output current measures 21.3 A, and the output voltage is 24.4 V. These values meet the converter's design specifications, demonstrating its capability to deliver the required power efficiently under full load conditions. The stable output voltage and current further validate the effectiveness of the interleaving technique in maintaining steady-state operation. On the input side, the current is recorded at 18.3 A with an input voltage of ~28.5 V. The slight discrepancy between the input voltage and the voltage across the MOSFETs can be attributed to inherent simulation assumptions and losses within the converter. However, this difference remains within acceptable limits, highlighting the converter's efficiency and minimal internal losses.

3.2 | Experimental Results of Two-Phase IBC

Building upon the simulation results and discussions of the two-phase IBC, this section provides experimental validation and its findings. The experimental setup aimed to corroborate the simulated performance characteristics of the converter and assess its practical implementation in charging a BESS. The experimental setup Figure 9 and extended Figure 10 involved two TSM-DE18M(II) solar panels connected in parallel to ensure sufficient power input to the buck converter.

To achieve reliable performance assessment, the CSA-based MPPT algorithm was tested using a standardized laboratory approach. Two parallel connections of TSM-DE18M(II) solar panels were used to start the experiment. To maximize exposure, these panels were properly angled using an adjustable solar panel platform. This allowed for a thorough assessment of

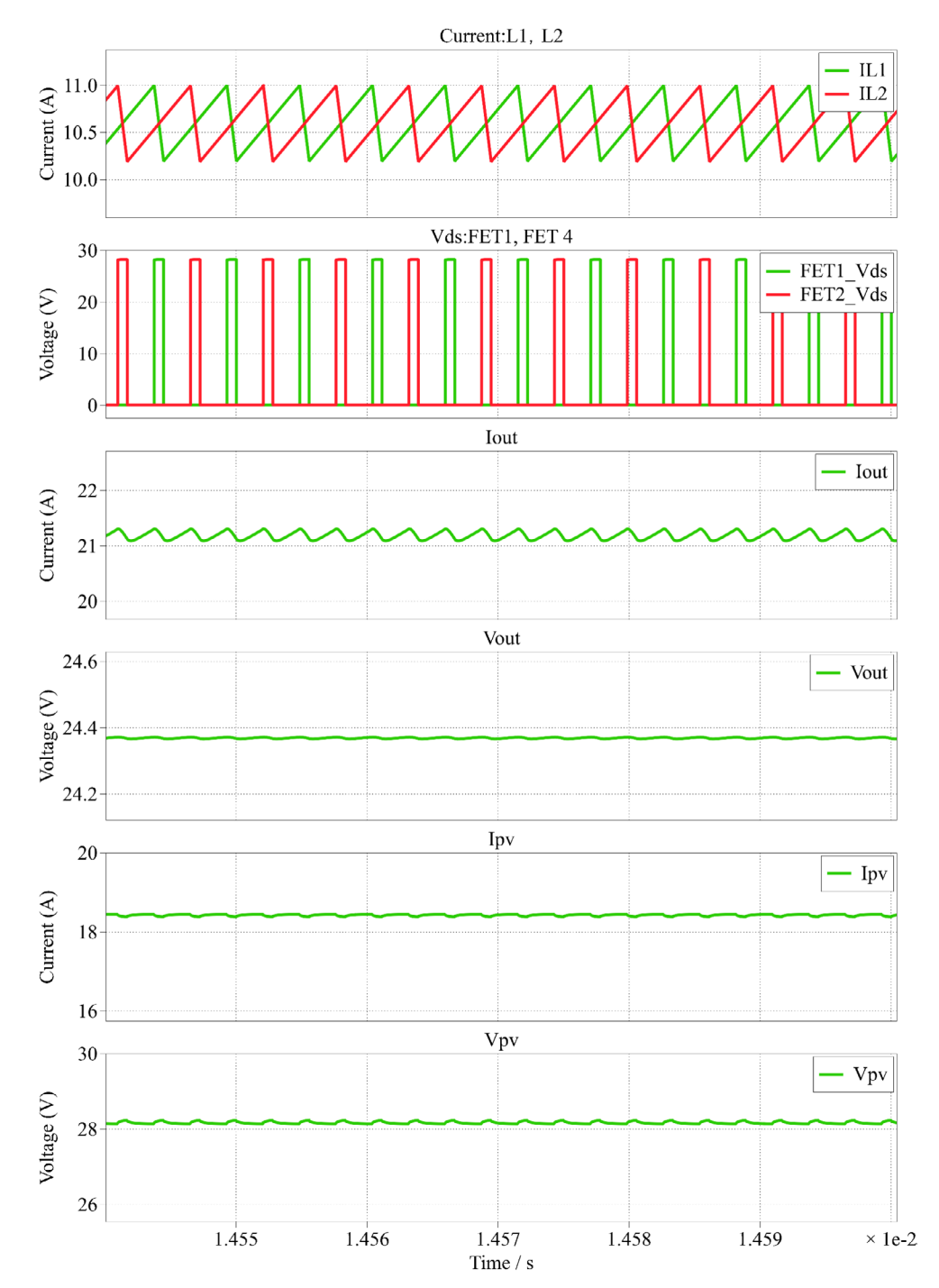


FIGURE 8 | Output characteristics of two-phase IBC at full load condition.

MPPT behavior in dynamic environmental conditions. Precision voltage and current sensors were incorporated into the system to precisely record the electrical properties of the solar panels. The panel V_{pv} and current I_{pv} were recorded by these sensors and then sent to a data-collecting system for monitoring and analysis in real-time.

The measured V_{pv} and I_{pv} values, as well as input parameters including temperature and irradiation, were used to initialize the CSA-based MPPT algorithm. Duty cycle values were dynamically optimized by the algorithm to guarantee optimal power extraction from the solar panels. The two-phase IBC then used the

calculated duty cycle values to accurately control the charging current that was supplied to the BESS by regulating the output voltage. The two-phase IBC was designed to produce an output of 24.4 V and 21.3 A, which was used to charge a 7S8P configuration of 18650 NMC lithium-ion batteries, each with a capacity of 2.6 Ah. The charging process was conducted under CC conditions, with a DT80 data logger employed to monitor and record the temperature of the BESS throughout the charging cycle.

Temperature monitoring was essential to evaluating thermal dynamics during the charging process in the experimental setup for charging the BESS using the two-phase IBC regulated by

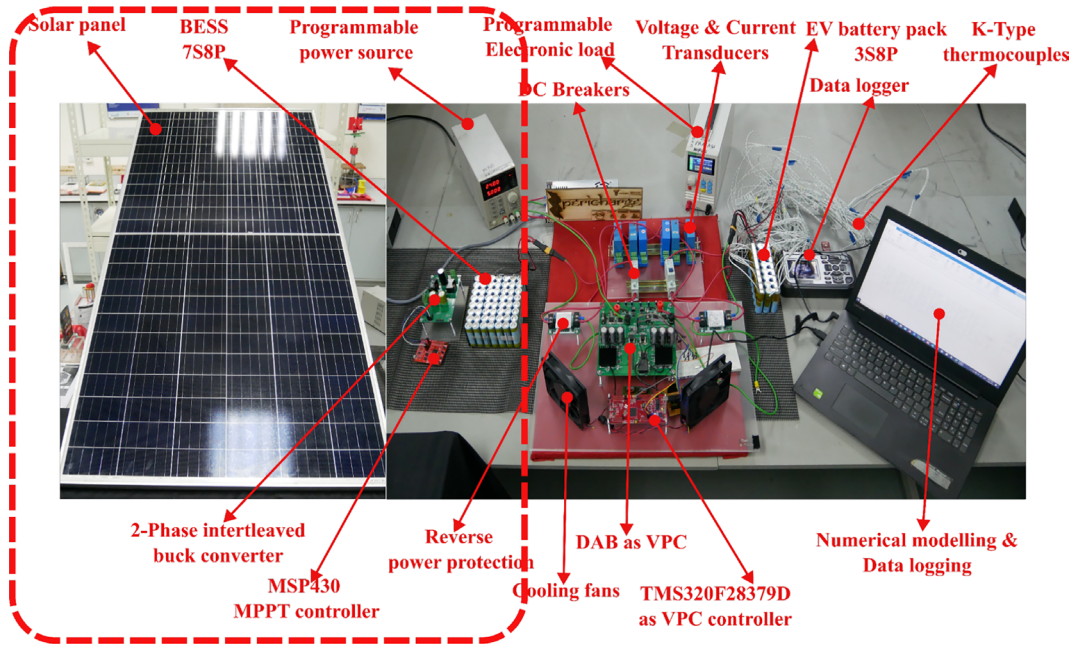
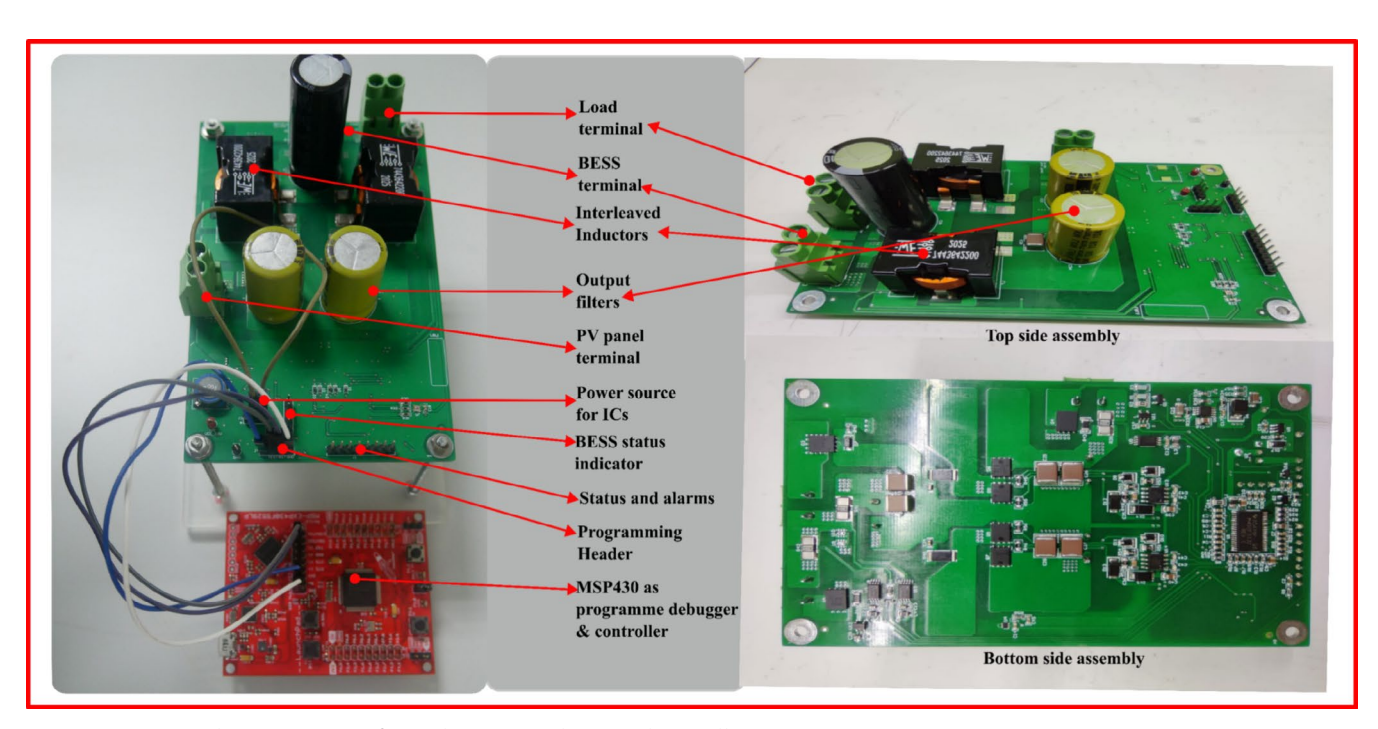


FIGURE 9 | Experimental setup for PV-BESS charging (dotted portion—PV-powered BESS charging system).



 $\textbf{FIGURE 10} \quad | \quad \text{Hardware prototype of two-phase IBC with external controller MSP430}.$

the CSA-based MPPT algorithm. The BESS's temperature was measured in real-time using a K-type thermocouple, which has a temperature range of -25°C to 125°C (-13°F to 257°F) and a tolerance of $\pm 1.5^{\circ}\text{C}$ ($\pm 2.7^{\circ}\text{F}$). The battery pack's thermocouple was positioned carefully to continually record temperature changes during the charging cycle. The battery system's thermal response under various operating situations was recorded by taking temperature readings at regular intervals using a DT80 data logger integrated into the system. With the IBC providing a steady output of 24.4V and 21.3 A, the charging profile—which was managed by CSA-generated duty cycles—ensured that the reference current profile was maintained.

To specify the operational limitations and environmental elements influencing the two-phase IBC and CSA-based MPPT system's performance in charging the BESS, the experiment's boundary conditions and results are set. When analyzing efficiency, thermal behavior, and control effectiveness, these circumstances guarantee accuracy and reproducibility.

To verify the effectiveness of the two-phase interleaved buck converter (IBC) and CSA-based MPPT in charging the BESS, the experimental setup's boundary conditions were established based on actual circumstances. To ensure live testing under naturally fluctuating sun irradiation and ambient temperatures, the

experiment's solar panels were two TSM-DE18M(II) units connected in parallel and positioned outside close to the lab. Instead of simulating irradiation, this method reflected real sun conditions, creating a dynamic and realistic input environment. Due to shifting weather patterns and the time of day, the panels were exposed to direct sunshine, with naturally fluctuating irradiation levels throughout the experiment. Continuous monitoring of the Vpv and Ipv outputs served as input parameters for the CSA algorithm, which dynamically modified the IBC's duty cycles to maximize power extraction. To ensure reliable charging of the 7S8P configuration of 18650 NMC lithium-ion batteries under a variety of circumstances, the converter was made to deliver a steady output voltage of 24.4V and a current of 21.3 A. A K-type thermocouple was used to track the battery pack's temperature during the charging cycle when the BESS was charged in constant current (CC) mode. With a temperature range of -25°C to 125°C and a tolerance of ±1.5°C, the thermocouple was linked to a DT80 data logger, which captured temperature changes in real-time environmental settings. By placing the solar panels outdoors, the system's ability to adjust to variations in natural irradiance was revealed, confirming the CSA algorithm's efficacy and the IBC's operational stability. A realistic assessment of performance parameters, such as tracking efficiency, dynamics, and converter stability under live settings, was made possible by these boundary conditions.

3.2.1 | PV and IV Characteristics

The I–V and P–V curves of the solar panels were plotted to understand their behavior under real-time operating conditions shown in Figures 11 and 12. These curves are crucial for determining the maximum power point (MPP) and ensuring efficient power transfer from the panels to the converter.

By analyzing these curves shown in Figure 13, can gain valuable insights into the operational behavior of the PV panels, including how irradiance and temperature fluctuations affect their voltage and current outputs. This understanding is crucial for optimizing the efficiency of solar energy systems and ensuring effective power conversion in conjunction with the two-phase IBC.

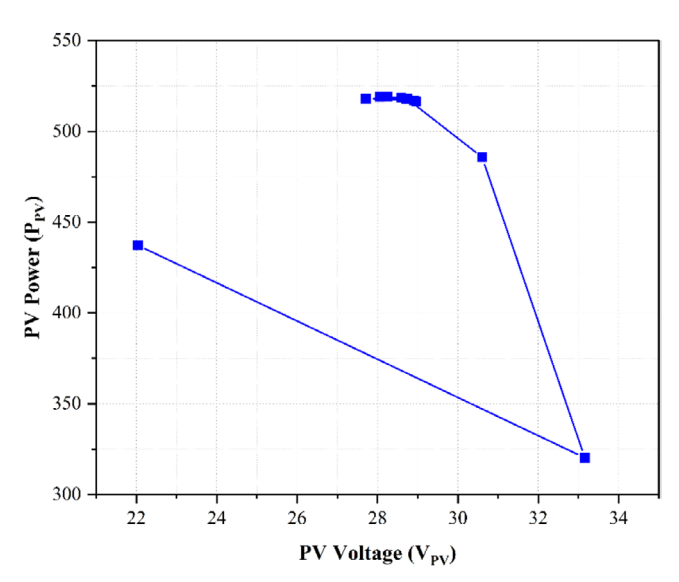


FIGURE 11 | PV characteristics of TSM-DE18M(II).

a. Time versus irradiance.

This curve plots the solar irradiance (measured in W/m^2) against time. It provides insights into the variation of sunlight intensity throughout the day. Key observations typically include:

- Peak Irradiance: The curve generally shows higher irradiance values during midday, reflecting the peak sunlight conditions.
- **Variation**: The irradiance fluctuates due to factors such as cloud cover or the angle of the sun, which impacts the amount of solar energy incident on the panels.
- b. Time versus ambient and PV temperature.

This curve shows the variation of ambient temperature and PV panel temperature over time. Important points to note include:

- Ambient Temperature: The ambient temperature tends to vary with the time of day, following a typical daily temperature cycle.
- **PV Temperature**: The PV panel temperature usually lags behind the ambient temperature due to heat absorption and dynamic dissipation. It often reaches higher temperatures than the ambient temperature, especially during peak sunlight hours.
- c. Irradiance versus PV voltage corresponding to PV temperature.

This curve plots the relationship between solar irradiance and the PV panel voltage, with PV temperature as a parameter. Observations typically include:

- **Voltage Response**: As irradiance increases, the PV voltage generally increases up to a certain point, reflecting higher energy input.
- **Temperature Influence**: Higher PV temperatures can lead to a decrease in voltage output due to the negative

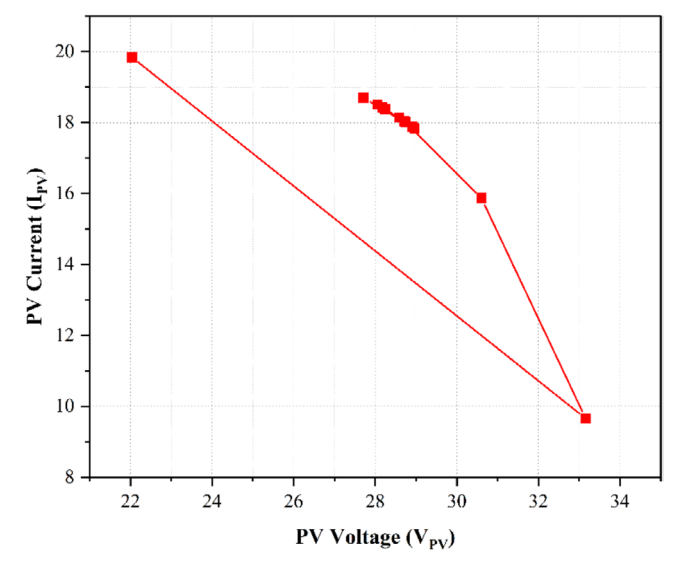


FIGURE 12 | IV Characteristics of TSM-DE18M(II).

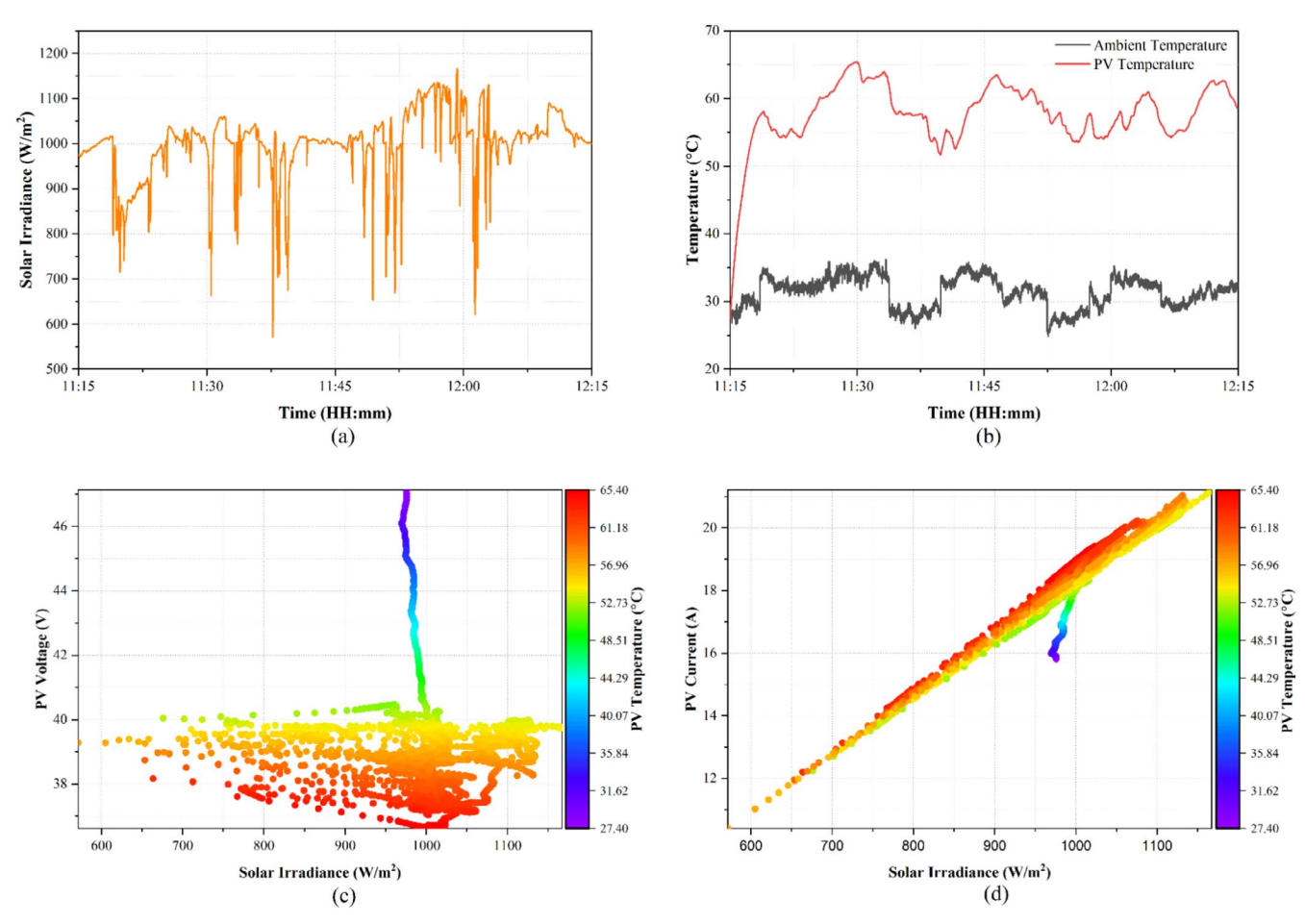


FIGURE 13 | Characteristics curves of (a) time versus irradiance, (b) time versus ambient and PV temperature, (c) irradiance versus PV voltage corresponding to PV temperature, and (d) irradiance versus PV current corresponding to PV temperature.

temperature coefficient of the PV cells. This curve helps to understand how temperature variations affect voltage under different irradiance levels.

d. Irradiance versus PV current corresponding to PV temperature.

This curve depicts the relationship between solar irradiance and PV panel current, again with PV temperature as a parameter. Key observations include:

- Current Response: The PV current usually increases with higher irradiance, as more sunlight results in higher current generation.
- Temperature Impact: The effect of temperature on current is less pronounced compared to voltage, but higher temperatures can still impact the efficiency and performance of the PV cells.

3.2.2 | Efficiency Analysis

To comprehensively evaluate the performance of the two-phase IBC converter in charging the BESS, an efficiency analysis compares simulated, theoretical, and experimental efficiency, providing a thorough assessment of the converter's performance under

full load conditions. Various losses across the components at full load conditions are presented in Table 7.

The data presented in Table 8 demonstrates that the simulation of a two-phase IBC exhibits high efficiency, particularly at higher power levels. The efficiency values indicate that the converter effectively handles and converts power from the PV system to the output load. The observed trend of increasing efficiency with input power and stabilizing efficiency at higher power levels highlights the converter's strong performance characteristics and reliability in practical applications.

3.2.2.1 | **Initial Efficiency.** At $V_{\rm PV} = 28.50\,\rm V$ and $I_{\rm PV} = 0.01\,\rm A$, output voltage and current are zero. This indicates that no significant power is being delivered or converted at this point. The system is in a no-load condition.

3.2.2.2 | Increasing Efficiency With Power. As the input power increases from 0.39 W to 307.85 W, there is a corresponding rise in both the output power and efficiency. This trend shows that the converter becomes more effective as more power is supplied to it. Efficiency rises from 0.85 to 0.95 as input power increases, reaching a peak efficiency of 0.95 at several power levels. This demonstrates that the converter performs very efficiently at higher power levels, effectively converting input power into usable output power.

3.2.2.3 | **Stable Efficiency at High Power Levels.** Efficiency values stabilize at around 0.94 to 0.95 for input powers exceeding ~255.58 W. This stability suggests that the converter maintains consistent performance and minimal losses under typical operating conditions, confirming the robustness of the converter design.

By examining experimental data given in Tables 9 and 10 We gain insights into the converter's ability to manage and minimize power losses across varying operating conditions, including input and output power, total power losses, and resulting efficiency. This analysis highlights the converter's robustness and efficiency, particularly at higher power levels, and validates its design for optimal performance in real-world scenarios. The following discussion delves into the correlation between total power losses and efficiency, comprehensively assessing the converter's effectiveness.

3.2.2.4 | Initial Data Point (High Losses, Zero Efficiency). At V_{PV} =28.42V and I_{PV} =0.00 A, no output power is delivered (0W). The total power loss is 0.88W, representing

TABLE 7 | Overall losses across the fundamental components of the converter

Quantity	Value	Unit
$P_{ON ext{-}H}$	1.80	W
$P_{\mathit{ON-L}}$	3.6	W
$P_{SW ext{-}H}$	0.571	W
$P_{SW\text{-}L}$	0.0057	W
P_{DIODE}	0.576	W
P_{COSS}	0.265	W
P_D	0.173	W
P_G	0.036	W
P_{IC}	0.0288	W
$P_{L(DCR)}$	1.20	W
P_{CIN}	1.07	W
P_{COUT}	0.00734	W
P_{OUT}	7.54	W

start-up or no-load losses, resulting in zero efficiency. This is expected as the converter is not effectively transferring power at such low levels.

3.2.2.5 | **Low Power Operation.** At low input power (168.74 W), the total power loss is 1.46 W. Despite the losses, the converter achieves an efficiency of 0.99, indicating that a significant portion of the input power is converted to output power. This discrepancy is likely due to non-ideal component behavior, such as switching losses and resistive losses, which are not fully accounted for in simulations.

3.2.2.6 | **High Power Operation.** At higher input powers, such as 337.24W and above, the total power loss continues to increase (3.47W at 331.24W input, 4.78W at 425.65W input, 6.35W at 494.67W input, and 7.54W at 530.29W input). Despite the increase in absolute losses, the efficiency remains high at around 0.99. The high efficiency at these levels demonstrates the converter's capability to manage power losses effectively, maintaining a minimal impact on overall performance even as input power increases significantly.

3.2.2.7 | **Efficiency and Losses Correlation.** The correlation between total power loss and efficiency reveals that while absolute losses increase with higher power levels, their relative impact diminishes. The converter is designed to handle high power with minimal efficiency degradation, reflecting its robust design and operational efficiency.

The analysis of total power losses with input power and efficiency underscores the efficiency of the two-phase IBC across varying power levels. The converter shows high efficiency at higher power levels, where total power losses represent a smaller fraction of the input power. These findings validate the converter's design and its effectiveness in minimizing losses while maintaining high efficiency, making it well-suited for practical applications requiring efficient power conversion. Overall, the comparison highlights the necessity of accounting for real-world inefficiencies in practical applications. While simulations provide a benchmark, experimental data gives a more accurate picture of the converter's performance, revealing the importance of thorough testing and consideration of all potential losses in design and analysis. The output power versus efficiency curve for all three modes of evaluation is shown in Figure 14.

TABLE 8 | Overall output data under varying load based on simulation.

V _{PV} (V)	I _{PV} (A)	V _o (V)	I _o (A)	R ₀ (Ohms)	P _{input} (W)	P _{output} (W)	Efficiency
28.50	0.01	0.00	0.00	0.00	0.39	0.00	0.00
28.24	5.06	24.20	5.00	4.84	143.04	121.00	0.85
28.36	7.29	24.28	8.00	3.04	206.66	194.24	0.94
28.42	8.99	24.15	10.00	2.42	255.58	241.50	0.94
28.54	10.79	24.32	12.00	2.03	307.85	291.84	0.95
28.32	13.59	24.37	15.00	1.62	384.81	365.55	0.95
28.57	16.35	24.40	18.00	1.36	467.24	439.20	0.94
28.50	18.30	24.40	21.30	1.15	521.55	519.72	0.99

TABLE 9 | Overall output data under varying loads with calculated component loss.

V _{PV} (V)	I _{PV} (A)	V _o (V)	I _o (A)	P _{input} (W)	P _{output} (W)	Total power loss (W)	Efficiency
28.42	0.00	0.00	0.00	0.00	0.00	0.88	0.00
28.60	5.90	24.00	5.00	168.74	120.00	1.46	0.99
28.85	7.50	24.15	8.00	216.38	193.20	2.16	0.99
28.27	9.80	24.30	10.00	277.05	243.00	2.73	0.99
28.58	11.80	24.32	12.00	337.24	291.84	3.47	0.99
28.76	14.80	24.37	15.00	425.65	365.55	4.78	0.99
28.79	17.20	24.40	18.00	494.67	439.20	6.35	0.99
28.82	18.40	24.48	20.00	530.29	489.60	7.54	0.98

TABLE 10 | Overall output data under varying load based on experiment.

VPV(V)	IPV(A)	Vo(V)	Io(A)	P _{input} (W)	P _{output} (W)	Efficiency
28.42	0.00	0.00	0.00	0.00	0.00	0.00
28.60	5.90	24.00	5.00	168.74	120.00	0.71
28.85	7.50	24.15	8.00	216.38	193.20	0.89
28.27	9.80	24.30	10.00	277.05	243.00	0.88
28.58	11.80	24.32	12.00	337.24	291.84	0.87
28.76	14.80	24.37	15.00	425.65	365.55	0.86
28.79	17.20	24.40	18.00	495.19	439.20	0.89
28.82	18.40	24.48	20.00	530.29	489.60	0.92

3.2.3 | Output Characteristics

The primary objective is to evaluate the performance of the two-phase IBC in managing the power conversion from solar panels to the BESS. The setup involves using solar panels to harness solar energy, which is then converted into a regulated DC voltage by the two-phase IBC. This converter is designed to enhance the efficiency and stability of the power transfer by interleaving two phases, which reduces output ripple and improves overall performance. The BESS, composed of lithium-ion batteries, is charged using the output of the converter, ensuring that the energy captured from the solar panels is stored efficiently for later use. The experiment aims to demonstrate the effectiveness of this configuration in maintaining optimal charging conditions, balancing the power flow, and improving the overall reliability and efficiency of the solar-powered energy system. The overall output characteristics of the system are shown in Figure 15.

3.2.4 | BESS Charging Characteristics

In this experiment, a BESS consisting of 7S8P of 18650 NMC lithium-ion cells, each with a nominal capacity of 2.6Ah, was supplied with a controlled charging current via a two-phase IBC. A 1C charging rate for the entire battery pack $(2.6Ah\times8$ parallel strings = $20.8Ah\approx21$ Ah) is shown by the IBC's output of 24.372V and 21.28A. In a standard lithium-ion charging technique, CC–CV A constant current is delivered by the CC phase to quickly raise

the SOC. The charger switches to the CV phase when the terminal voltage hits the top threshold, which is usually 4.2 V/cell for NMC. It maintains that voltage while lowering the current.

The charging cycle in our investigation, however, ended before it reached the CV phase. The charging process is carried out between SOCs 0.2 to 0.9, or terminal voltages below the full-charge voltage threshold (4.2 V/cell). At full charge, the full-pack voltage in a 7S arrangement is 29.4 V. Since the voltage was still within the safe linear charging range (i.e., less than 29.4 V) after the CC stage (0.9 SOC), the system did not need to switch to the CV phase. To maintain a simplified and thermally safer profile, the experiment purposefully avoids the CV phase. Avoid excessive heating brought on by high-voltage, low-current tail charging, which usually results in a slight improvement in SOC but significant thermal stress. To create an efficient passive cooling strategy, only examine the thermal behavior of BESS during high-current charging (i.e., CC phase).

The temperature increase and internal resistance losses can be attributed to several factors. Each cell possesses a finite internal resistance, causing power to dissipate as heat. At a 1C charging rate, this loss becomes significant and directly converts into heat. Additionally, the positive electrode (LiNiMnCoO₂) releases heat during charging due to exothermic intercalation reactions, which become particularly prominent at higher SOC levels, especially near 0.9. Switching harmonics and residual current ripple may also contribute slightly to the rise in battery temperature.

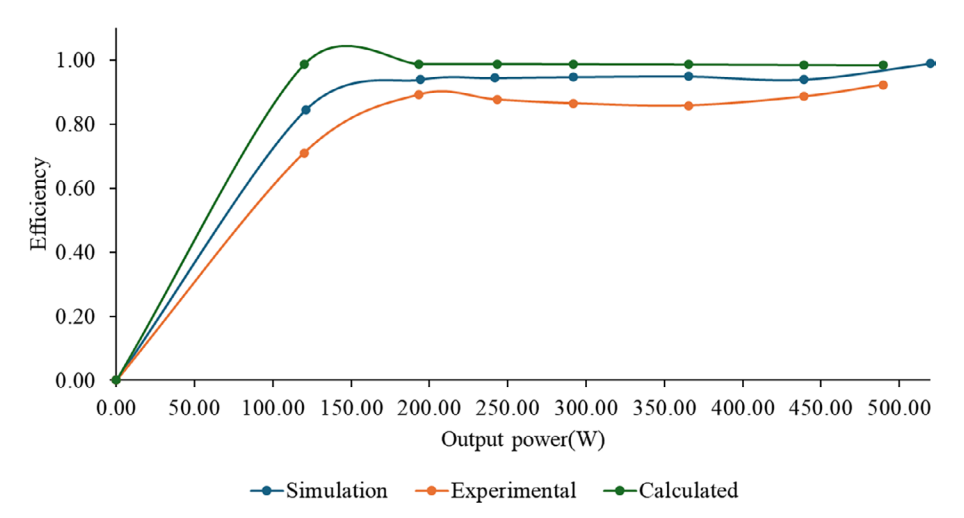


FIGURE 14 | Output power versus efficiency.

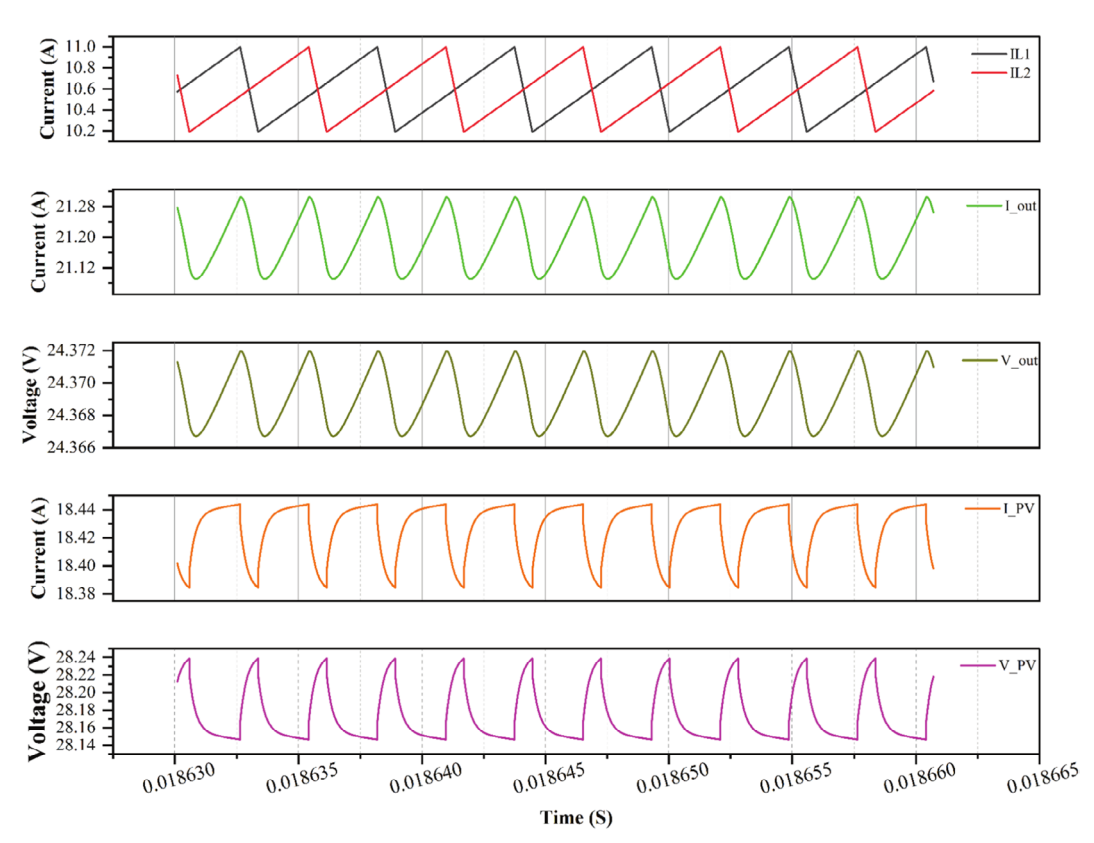


FIGURE 15 | Characteristics curves of time versus interleaved inductors currents, MOSFET Voltages, output current and voltage, input voltage.

The DT80 data logger recorded a significant temperature rise during the charging process. Starting from the ambient temperature of 27.25°C, the final temperature of the BESS reached 55.85°C by the end of the charging cycle. The results displayed in Table 11 and Figure 16 show the charging time and temperature rise under 1C conditions in charging the BESS demonstrating the efficacy of the two-phase IBC in maintaining stable output voltage and current, crucial for efficient and safe battery charging. The thermal analysis reveals that, under 1C charging conditions, the BESS experiences a substantial temperature rise, emphasizing the necessity for proper thermal management in high-rate charging scenarios.

3.2.5 | Uncertainty Analysis

An uncertainty analysis was carried out to guarantee the accuracy and consistency of the experimental findings acquired during the BESS charging procedure. A calibrated DT80 data logger was used to record all measurements for the experiment, which required charging a 7S8P NMC lithium-ion battery pack using a two-phase interleaved buck converter.

3.2.5.1 | **Voltage and Current Measurements.** To determine charging power and evaluate converter performance, voltage and current information were utilized.

TABLE 11 | Time taken to reach corresponding SOC with its rise in temperature.

SOC	0.2	0.3	0.4	0.5	0.6	0.7	0.8	0.9
Time	0.00	271	650	1027	1402	1781	2163	2637
Experimental temperature	27.25	32.40	37.61	42.39	46.76	50.49	54.02	55.85

Note: Green colour represents samll quantification, whereas, red shows lareg or high values and in between shades shows combination of the above mentioned.

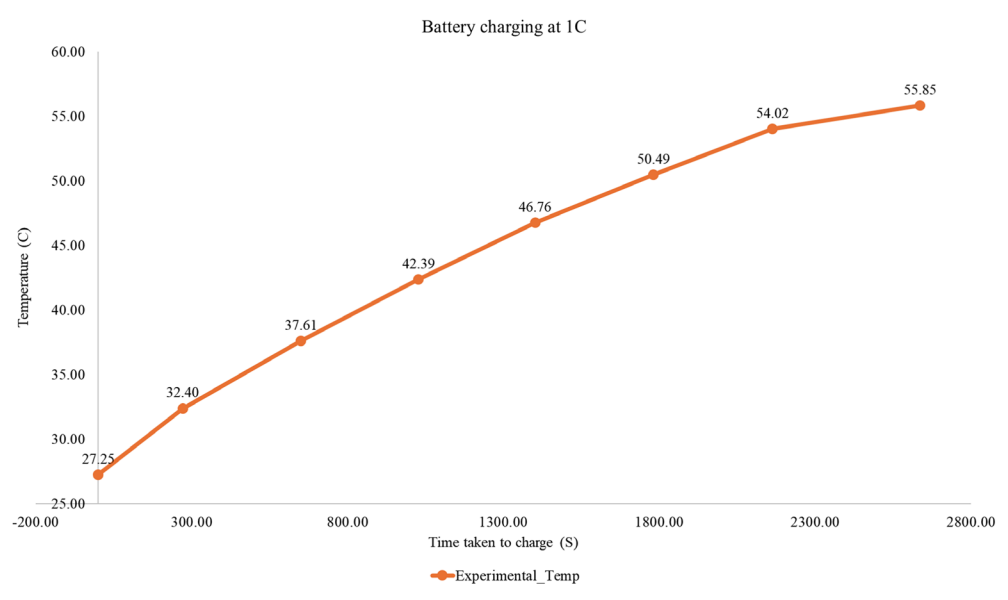


FIGURE 16 | Rise in temperature and charging time under 1C charging condition.

There is very little yet measurable uncertainty introduced by the DT80 logger when used in conjunction with calibrated voltage probes and Hall-effect current sensors. Depending on sensor calibration and wiring configuration, current measurements can have an inaccuracy of $\pm 1\%-2\%$, but voltage measurements typically have an accuracy of $\pm 0.2\%$. Using root-sum-square (RSS) propagation for uncertainty in power was estimated as 1.02%.

3.2.5.2 | **Temperature Measurement.** Battery temperature was recorded using thermocouples connected to the DT80 system. The sensors have a stated accuracy of $\pm 0.5^{\circ}$ C. Therefore, the initial temperature reading of 27.25°C could range from 26.75°C to 27.75°C, and the final reading of 55.85°C could range from 55.35°C to 56.35°C. This uncertainty, though relatively small, is significant when evaluating thermal thresholds for lithium-ion cells, especially as temperatures approach the upper safe operational limit (~60°C for NMC chemistry).

3.2.5.3 | **SOC Estimation.** A Coulomb counting technique based on the current integration over time was used to track the state of charge (SOC). Errors in capacity estimation and cumulative drift can affect this method. The SOC estimation uncertainty is anticipated to be between $\pm 3\%$ and 5% due to the battery pack's age, internal resistance variation, and absence of real-time voltage-SOC calibration.

3.2.5.4 | **Internal Resistance Estimation.** Internal resistance was not directly measured but inferred based on literature values and known thermal behavior. Since internal resistance

varies with SOC and temperature, the uncertainty in its estimation can be as high as $\pm 5\%$ –10% if not dynamically monitored.

Due to variations in enclosure effects and thermal mass, performance parameters like efficiency and thermal behavior might not extrapolate linearly to field-deployed systems, raising concerns about external scalability to higher power applications. Furthermore, differences in thermal efficiency under real-world conditions may result from the controlled indoor laboratory setting's lack of external stressors like changing ambient temperature, humidity, and airflow. Lastly, although benchmarking against traditional topologies is offered, more comprehensive comparative insights are limited due to the lack of real-time experimental comparisons conducted under the same conditions.

4 | Conclusion

In the context of charging a BESS, the simulation of the two-phase IBC under full load conditions provides insightful data on its performance. The output current of 21.28 A is distributed between the two inductors, with each inductor carrying an average current of ~11 A. This division of current highlights the effectiveness of the interleaving technique in balancing the load between the two phases. The results show that the inductor currents range from a lower value of 10.2 A to a higher value of 11.0 A. This variation, while present, is relatively small and indicates a well-managed distribution of current. The slight deviation in inductor currents from the nominal value of 11 A can be attributed to factors such as transient responses and minor

ripple effects inherent in practical operation. Despite these variations, the overall current distribution remains balanced, which is a key benefit of the interleaved design. By effectively managing the current ripple and balancing the load, the converter ensures stable and efficient operation.

The steady output voltage of 24.372V aligns precisely with the BESS's charging requirements. This regulated voltage was used to charge a 7S8P 18650 NMC lithium-ion battery pack, where each cell has a nominal capacity of 2.6 Ah. The BESS was charged under a constant current (CC) regime at 1C, from an initial SOC of 0.2 to 0.9, delivering a controlled and efficient charging cycle. The absence of a constant voltage (CV) phase ensured that the analysis remained focused on the thermal and electrical behavior of the CC region, which is critical for highefficiency applications. The balanced inductor currents and stable output voltage are indicative of the converter's ability to handle full load conditions efficiently while maintaining reliable performance.

Future work can focus on addressing the control complexity and computational overhead associated with the two-phase IBC and CSA for MPPT. Simplifying control methods for better current balancing between phases, without sacrificing performance, could enhance system efficiency. Additionally, optimizing the CSA for faster convergence in dynamic environments would improve realtime tracking under varying solar conditions. Lastly, improved thermal management strategies are necessary to address heat generation, ensuring more efficient and reliable charging of the BESS.

Nomenclature		HEVs	hybrid electric vehicles
EVs	electric vehicles	PEVs	plug-in electric vehicles
BEVs	battery electric vehicles	BESS	battery energy storage systems
PV	photovoltaic	MPPT	maximum power point tracking
IBC	interleaved buck converter	P&O	perturb and observe
LDR	light-dependent resistors	FOCV	fractional open-circuit voltage
IC	incremental conductance	HC	hill climbing
CV	constant voltage	SCC	short circuit current
MPC	model predictive control	FLC	fuzzy logic control
OCV	open circuit voltage	GWO	gray wolf optimization
PSO	particle swarm optimization	ABC	artificial bee colony
ACO	ant colony optimization	ANN	artificial neural network
SMC	sliding mode control	FPSO	fuzzy particle, swarm, optimization
DISMC	double integral, sliding mode, control	IBC	interleaved buck converter
ANFIS	adaptive, neuro-fuzzy, inference system	PCB	printed circuit board
CSA	cuckoo search algorithm	PWM	pulse-width modulated
ADC	analog-to-digital converter	NMC	nickle manganese cobalt
MCU	micro controller unit	AC	alternate current
CC	constant current	DCR	DC resistance
DC	direct current	RMS	root mean square
ESR	equivalent series resistance	В	power-law index
V_{j}	voltage of Jth particle at respective iteration	Υ	integral gamma function.
K	and step coefficient	$R_{\mathit{ON-H}}$	High-side MOSFET on-resistance $[\Omega]$

I_{batt}	output battery current [A]
R_{ON-L}	low-side MOSFET on-resistance $[\Omega]$
V_{batt}	output voltage [V]
I_V	Inductor current bottom [A]
R_{ON-L}	low-side MOSFET on-resistance $[\Omega]$
f_{sw}	switching frequency [Hz]
I_{batt}	output current [A]
$t_{f ext{-}H}$	high-side MOSFET fall time [sec]
t _{r-L}	low-side MOSFET rise time [ec]
I_{RR}	peak value of body diode reverse recovery current [A]
C_{OSS-H}	high-side MOSFET output capacitance [F]
$C_{GD ext{-}H}$	high-side MOSFET gate-drain capacitance [F]
t_{Df}	dead time for falling [sec]
Q_{g-L}	gate charge of low-side MOSFET [C]
C_{GS-L}	gate capacitance of low-side MOSFET [F]
I_{CC}	IC current consumption [A]
$I_{CAP}(RMS)$	RMS current of capacitor [A]
$\varDelta I_L$	ripple current of inductor
$P_{\mathit{ON-L}}$	conduction loss of low-side MOSFET [W]
$P_{SW\text{-}L}$	switching loss of low-side MOSFET [W]
P_{COSS}	output capacitance loss of MOSFET [W]
P_G	gate charge loss [W]
$P_{L(DCR)}$	conduction loss of inductor [W]
P_{COUT}	output capacitor loss [W]
HEVs	hybrid electric vehicles
PEVs	plug-in electric vehicles
BESS	battery energy storage systems
MPPT	maximum power point tracking
P&O	perturb and observe
FOCV	fractional open-circuit voltage
HC	hill climbing
SCC	short circuit current
FLC	fuzzy logic control
GWO	gray wolf optimization
ABC	artificial bee colony
ANN	artificial neural network
FPSO	fuzzy particle, swarm, optimization
IBC	interleaved buck converter
PCB	printed circuit board
PWM	pulse-width modulated
NMC	nickle manganese cobalt
AC	alternate current

V_{pv}	input voltage [V]
I_P	inductor current peak [A]
$R_{ON ext{-}H}$	high-side MOSFET on-resistance $[\Omega]$
$\varDelta I_L$	ripple current of inductor [A]
L	inductance value [H]
$t_{r ext{-}H}$	high-side MOSFET rise time [sec]
V_{D}	forward direction voltage of low-side MOSFET body diode $\left[V\right]$
$t_{\text{f-L}}$	low-side MOSFET fall time [sec]
t_{RR}	body diode reverse recovery time
C_{DS-H}	high-side MOSFET drain-source capacitance [F]
t_{Dr}	dead time for rising [sec]
Q_{g-H}	gate charge of high-side MOSFET [C]
C_{GS-H}	gate capacitance of high-side MOSFET [F]
V_{gs}	gate drive voltage [V]
DCR	inductor direct current resistance $[\Omega]$
ESR	equivalent series resistance of capacitor $[\Omega]$
$P_{ON ext{-}H}$	conduction loss of high-side MOSFET [W]
$P_{SW ext{-}H}$	switching loss of high-side MOSFET [W]
P_{DIODE}	reverse recovery loss of body diode [W]

Acknowledgments

 P_D

 P_{IC}

 P_{CIN}

This work was supported by Taylor's University through its Taylor's PhD SCHOLARSHIP Programme through grant TUFR/2017/001/01.

Conflicts of Interest

The authors declare no conflicts of interest.

dead time loss [W]

IC operation loss [W]

total power loss [W]

input capacitor loss [W]

Data Availability Statement

The data that support the findings of this study are available from the corresponding author upon reasonable request.

References

- 1. D. Vilcins, R. C. Christofferson, J.-H. Yoon, et al., "Updates in Air Pollution: Current Research and Future Challenges," *Annals of Global Health* 90, no. 1 (2024): 1–12, https://doi.org/10.5334/aogh.4363.
- 2. M. Muratori, M. Alexander, D. Arent, et al., "The Rise of Electric Vehicles-2020 Status and Future Expectations," *Progress in Energy* 3, no. 2 (2021): 022002, https://doi.org/10.1088/2516-1083/abe0ad.
- 3. A. J. Niri, G. A. Poelzer, S. E. Zhang, J. Rosenkranz, M. Pettersson, and Y. Ghorbani, "Sustainability Challenges Throughout the Electric Vehicle Battery Value Chain," *Renewable & Sustainable Energy Reviews* 191, no. December 2023 (2024): 114176, https://doi.org/10.1016/j.rser. 2023.114176.
- 4. P. Barman, L. Dutta, S. Bordoloi, et al., "Renewable Energy Integration With Electric Vehicle Technology: A Review of the Existing Smart Charging Approaches," *Renewable & Sustainable Energy Reviews* 183, no. June (2023): 113518, https://doi.org/10.1016/j.rser.2023. 113518.

- 5. F. Vignola, Z. Derocher, J. Peterson, et al., "Effects of Changing Spectral Radiation Distribution on the Performance of Photodiode Pyranometers," *Solar Energy* 129 (2016): 224–235, https://doi.org/10.1016/j.solen er.2016.01.047.
- 6. G. M. Yagli, D. Yang, and D. Srinivasan, "Automatic Hourly Solar Forecasting Using Machine Learning Models," *Renewable & Sustainable Energy Reviews* 105 (2019): 487–498, https://doi.org/10.1016/j.rser. 2019.02.006.
- 7. S. I. Vagropoulos, E. G. Kardakos, C. K. Simoglou, A. G. Bakirtzis, and J. P. S. Catalão, "ANN-Based Scenario Generation Methodology for Stochastic Variables of Electric Power Systems," *Electric Power Systems Research* 134 (2016): 9–18, https://doi.org/10.1016/j.epsr.2015.
- 8. J. Ahmed and Z. Salam, "An Improved Perturb and Observe (P&O) Maximum Power Point Tracking (MPPT) Algorithm for Higher Efficiency," *Applied Energy* 150 (2015): 97–108, https://doi.org/10.1016/j.apenergy.2015.04.006.
- 9. A. Safari and S. Mekhilef, "Simulation and Hardware Implementation of Incremental Conductance MPPT With Direct Control Method Using Cuk Converter," *IEEE Transactions on Industrial Electronics* 58, no. 4 (2011): 1154–1161, https://doi.org/10.1109/TIE.2010.2048834.
- 10. T. W. Hsu, H. H. Wu, D. L. Tsai, and C. L. Wei, "Photovoltaic Energy Harvester With Fractional Open-Circuit Voltage Based Maximum Power Point Tracking Circuit," *IEEE Transactions on Circuits and Systems II: Express Briefs* 66, no. 2 (2019): 257–261, https://doi.org/10.1109/TCSII.2018.2838672.
- 11. M. Lasheen, A. K. A. Rahman, M. Abdel-Salam, and S. Ookawara, "Performance Enhancement of Constant Voltage Based MPPT for Photovoltaic Applications Using Genetic Algorithm," *Energy Procedia* 100 (2016): 217–222, https://doi.org/10.1016/j.egypro.2016.10.168.
- 12. V. Jately, B. Azzopardi, J. Joshi, B. Venkateswaran, A. Sharma, and S. Arora, "Experimental Analysis of Hill-Climbing MPPT Algorithms Under Low Irradiance Levels," *Renewable and Sustainable Energy Reviews* 150 (2021): 111467, https://doi.org/10.1016/j.rser.2021.111467.
- 13. A. Lashab, D. Sera, and J. M. Guerrero, "A Dual-Discrete Model Predictive Control-Based MPPT for PV Systems," *IEEE Transactions on Power Electronics* 34, no. 10 (2019): 9686–9697, https://doi.org/10.1109/TPEL.2019.2892809.
- 14. X. Li, H. Wen, Y. Hu, and L. Jiang, "A Novel Beta Parameter Based Fuzzy-Logic Controller for Photovoltaic MPPT Application," *Renewable Energy* 130 (2019): 416–427, https://doi.org/10.1016/j.renene.2018.06.071.
- 15. W. M. Lin, C. M. Hong, and C. H. Chen, "Neural-Network-Based MPPT Control of a Stand-Alone Hybrid Power Generation System," *IEEE Transactions on Power Electronics* 26, no. 12 (2011): 3571–3581, https://doi.org/10.1109/TPEL.2011.2161775.
- 16. M. S. Jamri, A. M. Kassim, and M. R. Hashim, "A Voltage Mode Control Maximum Power Point Tracking for Stand-Alone Photovoltaic System," *Applied Mechanics and Materials* 313–314 (2013): 503–507, https://doi.org/10.4028/www.scientific.net/AMM.313-314.503.
- 17. S. Hosseini, S. Taheri, M. Farzaneh, and H. Taheri, "A High-Performance Shade-Tolerant MPPT Based on Current-Mode Control," *IEEE Transactions on Power Electronics* 34, no. 10 (2019): 10327–10340, https://doi.org/10.1109/TPEL.2019.2894528.
- 18. V. Jately and S. Arora, "Performance Investigation of Hill-Climbing MPPT Techniques for PV Systems Under Rapidly Changing Environment," in *Advances in Intelligent Systems and Computing*, vol. 624, ed. R. Singh, S. Choudhury, and A. Gehlot (Springer Singapore, 2018), 1145–1157, https://doi.org/10.1007/978-981-10-5903-2_120.
- 19. V. R. Kota and M. N. Bhukya, "A Novel Linear Tangents Based P&O Scheme for MPPT of a PV System," *Renewable and Sustainable Energy Reviews* 71 (2017): 257–267, https://doi.org/10.1016/j.rser. 2016.12.054.

- 20. M. A. Danandeh and G. S. M. Mousavi, "Comparative and Comprehensive Review of Maximum Power Point Tracking Methods for PV Cells," *Renewable & Sustainable Energy Reviews* 82, no. November 2016 (2018): 2743–2767, https://doi.org/10.1016/j.rser.2017.10.009.
- 21. H. Renaudineau, F. Donatantonio, J. Fontchastagner, et al., "A PSO-Based Global MPPT Technique for Distributed PV Power Generation," *IEEE Transactions on Industrial Electronics* 62, no. 2 (2015): 1047–1058, https://doi.org/10.1109/TIE.2014.2336600.
- 22. K. Atici, I. Sefa, and N. Altin, "Grey Wolf Optimization Based MPPT Algorithm for Solar PV System With SEPIC Converter," in *Proceedings 2019 4th International Conference on Power Electronics and Their Applications, ICPEA 2019* (IEEE, 2019), 1–6, https://doi.org/10.1109/ICPEA1. 2019.8911159.
- 23. R. K. Phanden, L. Sharma, J. Chhabra, and H. I. Demir, "A Novel Modified Ant Colony Optimization Based Maximum Power Point Tracking Controller for Photovoltaic Systems," *Materials Today: Proceedings* 38 (2020): 89–93, https://doi.org/10.1016/j.matpr.2020.06.020.
- 24. A. M. Eltamaly, "An Improved Cuckoo Search Algorithm for Maximum Power Point Tracking of Photovoltaic Systems Under Partial Shading Conditions," *Energies* 14, no. 4 (2021): 953, https://doi.org/10.3390/en14040953.
- 25. C. Gonzalez-Castano, C. Restrepo, S. Kouro, and J. Rodriguez, "MPPT Algorithm Based on Artificial Bee Colony for PV System," *IEEE Access* 9 (2021): 43121–43133, https://doi.org/10.1109/ACCESS.2021. 3066281.
- 26. W. Xiao, W. G. Dunford, P. R. Palmer, and A. Capel, "Application of Centered Differentiation and Steepest Descent to Maximum Power Point Tracking," *IEEE Transactions on Industrial Electronics* 54, no. 5 (2007): 2539–2549, https://doi.org/10.1109/TIE.2007.899922.
- 27. S. Benhadouga, A. Belkaid, I. Colak, M. Meddad, and A. Eddiai, "Experimental Validation of the Sliding Mode Controller to Improve the Efficiency of the MPPT Solar System," in 10th IEEE International Conference on Renewable Energy Research and Applications, ICRERA 2021 (IEEE, 2021), 333–337, https://doi.org/10.1109/ICRERA52334. 2021.9598584.
- 28. R. B. Roy, M. Rokonuzzaman, N. Amin, et al., "A Comparative Performance Analysis of ANN Algorithms for MPPT Energy Harvesting in Solar PV System," *IEEE Access* 9 (2021): 102137–102152, https://doi.org/10.1109/ACCESS.2021.3096864.
- 29. R. Ramaprabha, M. Balaji, and B. L. Mathur, "Maximum Power Point Tracking of Partially Shaded Solar PV System Using Modified Fibonacci Search Method With Fuzzy Controller," *International Journal of Electrical Power & Energy Systems* 43, no. 1 (2012): 754–765, https://doi.org/10.1016/j.ijepes.2012.06.031.
- 30. R. Pradhan and B. Subudhi, "Double Integral Sliding Mode MPPT Control of a Photovoltaic System," *IEEE Transactions on Control Systems Technology* 24, no. 1 (2016): 285–292, https://doi.org/10.1109/TCST.2015.2420674.
- 31. N. Priyadarshi, S. Padmanaban, P. K. Maroti, and A. Sharma, "An Extensive Practical Investigation of FPSO-Based MPPT for Grid Integrated PV System Under Variable Operating Conditions With Anti-Islanding Protection," *IEEE Systems Journal* 13, no. 2 (2019): 1861–1871, https://doi.org/10.1109/JSYST.2018.2817584.
- 32. F. Khosrojerdi, S. Taheri, and A. M. Cretu, "An Adaptive Neuro-Fuzzy Inference System-Based MPPT Controller for Photovoltaic Arrays," in 2016 IEEE Electrical Power and Energy Conference, EPEC 2016 (IEEE, 2016), 1–6, https://doi.org/10.1109/EPEC.2016.7771794.
- 33. S. Mohanty, B. Subudhi, and P. K. Ray, "A New MPPT Design Using Grey Wolf Optimization Technique for Photovoltaic System Under Partial Shading Conditions," *IEEE Transactions on Sustainable Energy* 7, no. 1 (2016): 181–188, https://doi.org/10.1109/TSTE.2015.2482120.
- 34. S. Figueiredo, R. N. A. Leao, and E. S. Aquino, "Hybrid MPPT Technique PSO-P&O Applied to Photovoltaic Systems Under Uniform and

- Partial Shading Conditions," *IEEE Latin America Transactions* 19, no. 10 (2021): 1610–1617, https://doi.org/10.1109/TLA.2021.9477222.
- 35. K. Y. Yap, C. R. Sarimuthu, and J. M. Y. Lim, "Artificial Intelligence Based MPPT Techniques for Solar Power System: A Review," *Journal of Modern Power Systems and Clean Energy* 8, no. 6 (2020): 1043–1059, https://doi.org/10.35833/MPCE.2020.000159.
- 36. D. A. Elalfy, E. Gouda, M. F. Kotb, V. Bureš, and B. E. Sedhom, "Comprehensive Review of Energy Storage Systems Technologies, Objectives, Challenges, and Future Trends," *Energy Strategy Reviews* 54 (2024): 1–27, https://doi.org/10.1016/j.esr.2024.101482.
- 37. A. Ali, H. H. H. Mousa, M. F. Shaaban, M. A. Azzouz, and A. S. A. Awad, "A Comprehensive Review on Charging Topologies and Power Electronic Converter Solutions for Electric Vehicles," *Journal of Modern Power Systems and Clean Energy* 12, no. 3 (2024): 675–694, https://doi.org/10.35833/MPCE.2023.000107.
- 38. P. Dini, S. Saponara, and A. Colicelli, "Overview on Battery Charging Systems for Electric Vehicles," *Electronics* 12, no. 20 (2023): 1–36, https://doi.org/10.3390/electronics12204295.
- 39. J. Chen, C. Yang, S. Tang, and J. Zou, "A High Power Interleaved Parallel Topology Full-Bridge LLC Converter for off-Board Charger," *IEEE Access* 9 (2021): 157790–157799, https://doi.org/10.1109/ACCESS. 2021.3130051.
- 40. P. Muthukumar, M. Venkateshkumar, and C. S. Chin, "A Comparative Study of Cutting-Edge Bi-Directional Power Converters and Intelligent Control Methodologies for Advanced Electric Mobility," *IEEE Access* 12, no. February (2024): 28710–28752, https://doi.org/10.1109/ACCESS.2024.3360267.
- 41. L. Li, G. Xu, D. Sha, Y. Liu, Y. Sun, and M. Su, "Review of Dual-Active-Bridge Converters With Topological Modifications," *IEEE Transactions on Power Electronics* 38, no. 7 (2023): 9046–9076, https://doi.org/10.1109/TPEL.2023.3258418.
- 42. M. Amir, I. Ahmad, M. Waseem, and M. Tariq, "A Critical Review of Compensation Converters for Capacitive Power Transfer in Wireless Electric Vehicle Charging Circuit Topologies," *Green Energy and Intelligent Transportation* 4, no. 2 (2025): 100196, https://doi.org/10.1016/j.geits.2024.100196.
- 43. S. Pragaspathy, R. V. D. R. Rao, V. Karthikeyan, R. Bhukya, P. K. Nalli, and K. N. S. D. P. Korlepara, "Analysis and Appropriate Choice of Power Converters for Electric Vehicle Charging Infrastructure," in 2022 Second International Conference on Artificial Intelligence and Smart Energy (ICAIS) (IEEE, 2022), 1554–1558, https://doi.org/10.1109/ICAIS 53314.2022.9742853.
- 44. I. N. Jiya, A. Salem, H. van Khang, and R. Pomarnacki, "Integrated Multiport DC-DC and Multilevel Converters for Multiple Renewable Energy Source Integration," *IEEE Access* 11, no. October (2023): 132483–132495, https://doi.org/10.1109/ACCESS.2023.3336567.
- 45. A. Jain and S. Bhullar, "An Extensive Analysis of Power Converter Architectures for Grid-Connected Solar Photovoltaic Driven Electric Vehicles (EVs)," *Engineering Science & Technology, an International Journal* 58, no. August (2024): 1–15, https://doi.org/10.1016/j.jestch. 2024.101841.
- 46. D. G. Wilhelm and L. Universität, Design and Control of a Multiphase Interleaving DC-DC Converter With Loss Optimizing Operating Strategies for Electric Vehicle (2023).
- 47. V. N. Saraswathi and V. P. Ramachandran, "A Comprehensive Review on Charger Technologies, Types, and Charging Stations Models for Electric Vehicles," *Heliyon* 10, no. 20 (2024): e38945, https://doi.org/10.1016/j.heliyon.2024.e38945.
- 48. D. U. Kim, D. Dong, B. Kim, and S. Kim, "A New Asymmetric Leakage Inductance for Enhancing Zero-Voltage Switching Performance in Asymmetric Triple-Active-Bridge Converters," *IEEE Transactions on Power Electronics* 39, no. 9 (2024): 11187–11203, https://doi.org/10.1109/TPEL.2024.3405935.

- 49. L. Gevorkov, J. L. Domínguez-García, L. T. Romero, and À. F. Martínez, "Modern MultiPort Converter Technologies: A Systematic Review," *Applied Sciences* 13, no. 4 (2023): 2579, https://doi.org/10.3390/app13042579.
- 50. X. S. Yang and S. Deb, "Cuckoo Search via Lévy Flights. 2009 World Congr," in *Proceeding of World Congress on Nature & Biologically Inspired Computing (NaBIC 2009)* (IEEE, 2009), 210–214.
- 51. K. S. P. Oruganti, C. A. Vaithilingam, G. Rajendran, A. Ramasamy, and R. A. Gamboa, "Performance Evaluation of Maximum Power Point Algorithms for Annulling the Effect of Irradiance and Temperature for Standalone Electric Vehicle Charger," in 3rd IEEE International Virtual Conference on Innovations in Power and Advanced Computing Technologies, i-PACT 2021 (IEEE, 2021), 1–6, https://doi.org/10.1109/i-PACT5 2855.2021.9696741.
- 52. L. ROHM Co., "Efficiency of Buck Converter," *Application Note* 2021, no. December (2016): 1–16.